

Arnold tongue entrainment reveals dynamical principles of the embryonic segmentation clock

Paul Gerald Layague Sanchez^{a,d,h}, Victoria Mochulska^b, Christian Mauffette Denis^b, Gregor Mönke^{a,e}, Takehito Tomita^{a,h}, Nobuko Tsuchida-Straeten^{a,f}, Yvonne Petersen^{c,f}, Katharina F. Sonnen^{a,g}, Paul François^b, and Alexander Aulehla^a✉

^aEuropean Molecular Biology Laboratory (EMBL), Developmental Biology Unit, Meyerhofstraße 1, 69117 Heidelberg, Germany
^bMcGill University, H3A 2T8 Montréal, Canada

^cEuropean Molecular Biology Laboratory (EMBL), Transgenic Service, Meyerhofstraße 1, 69117 Heidelberg, Germany

^dPresent address: Department of Genetics and Evolution, University of Geneva, 1205 Geneva, Switzerland

^ePresent address: Hubrecht Institute 3584 CT Utrecht, The Netherlands

^fPresent address: Ernst Strüngmann Institute for Neuroscience, 60528 Frankfurt am Main, Germany

^gPresent address: Universitätsklinikum Heidelberg, 69120 Heidelberg, Germany

^hCollaboration for joint PhD degree between EMBL and Heidelberg University, Faculty of Biosciences, 69120 Heidelberg, Germany

1 **Living systems exhibit an unmatched complexity, due to count-**
2 **less and entangled interactions across scales. Here we aim to**
3 **understand and gain control of a complex system, such as the**
4 **segmentation timing of a developing mouse embryo, without a**
5 **reference to these detailed interactions. To this end, we develop**
6 **a coarse-grained approach in which theory guides the experi-**
7 **mental identification of the system-level responses to entrain-**
8 **ment, in the context of a network of coupled cellular oscillators**
9 **that constitute the embryonic somite segmentation clock.**

10 **We demonstrate period- and phase-locking of the embryonic**
11 **system across a wide range of entrainment parameters, includ-**
12 **ing higher-order coupling. These experimental quantifications**
13 **allow to derive the phase response curve (PRC) and Arnold**
14 **tongues of the system, revealing the essential dynamical prop-**
15 **erties of the embryonic segmentation clock. Our results indicate**
16 **that at the macro-scale, the somite segmentation clock has char-**
17 **acteristics of a highly non-linear oscillator close to a saddle-node**
18 **on invariant cycle (SNIC) bifurcation and suggests the presence**
19 **of long-term feedbacks.**

20 **Combined, this coarse-grained theoretical-experimental ap-**
21 **proach reveals how we can derive simple, essential features of**
22 **a highly complex dynamical system and hereby provides precise**
23 **experimental control over the pace and rhythm of the somite**
24 **segmentation clock.**

25 **entrainment | oscillations | somitogenesis | presomitic mesoderm (PSM)**

26 **Correspondence: aulehla@embl.de**

27 Introduction

28 How do we gain insight into a complex system, which ex-
29 hibits emergent properties that reflect the integration of en-
30 tangled interactions and feedback regulation? As pointed out
31 in the late 1970s by David Marr and Tomaso Poggio in their
32 seminal paper (2), understanding the complexity encountered
33 when studying the "nervous system or a developing embryo"
34 requires the analysis at multiple levels of organization. Their
35 core tenet is that also in biological systems, different levels of
36 organization, while obviously causally linked, exhibit only a
37 loose connection and importantly, can be studied and under-
38 stood independently from each other.

39 Such observations are not specific to biology and have been
40 made more quantitative in other fields. In physics, renormal-
41 ization techniques coarse-grain degrees of freedom to obtain

scale-free theories, allowing to define universality classes in-
dependent of the precise details of interactions (3, 4). An-
other recent example is the parameter space compression the-
ory, showing how complex systems (in biology or physics)
can be typically reduced to simpler descriptions with few pa-
rameters (5–7).

Going one step further, this suggests that one might be able
to study- and control- complex systems provided we identify
the essential, macro-level behaviour. This is possible because
only a limited number of universal descriptions exists, with
defining behaviours and properties, that do not depend on the
detailed implementation. A central challenge that remains is
to implement these theoretical ideas to the experimental study
of biological complexity.

Here, we develop a coarse-grained approach combining the-
ory and experiments to study a cellular oscillator ensemble
that constitutes the embryonic somite segmentation clock.
Functionally, this clock controls the periodic formation of
somites, the precursor of the vertebral column and other tis-
sues (8, 9). Molecularly, the segmentation clock comprises
the oscillatory activity of several major signaling pathways,
such as the Notch, Wnt and Fgf signaling pathways, which
show oscillatory dynamics with a period matching somite
formation, i.e. ~2 hours in mouse embryos (10–14). More
recently, segmentation clock oscillations with a period of ~5
hours have been identified in human induced pluripotent stem
cells (iPSCs) differentiated into paraxial mesoderm, identify-
ing a set of ~200 oscillating genes, including targets of Notch
and Wnt signaling. (15–17).

Strikingly, as individual oscillating cells are coupled to their
neighbours via Notch-Delta signaling, the oscillations occur
synchronized and wave-like activity patterns appear to peri-
odically sweep along the embryonic anterior-posterior axis
(14, 18–23).

Adding to the complexity, these periodic spatiotemporal
wave patterns are linked to an underlying spatial period gradi-
ent along the embryonic axis, i.e. signaling dynamics in cells
close to the posterior of the embryo oscillate faster compared
to those in cells located more anteriorly. Such a period gra-
dient linked to the segmentation clock has been identified in
several species (24–30) and also in in vitro assays culturing
intact or even dissociated PSM (27, 29).

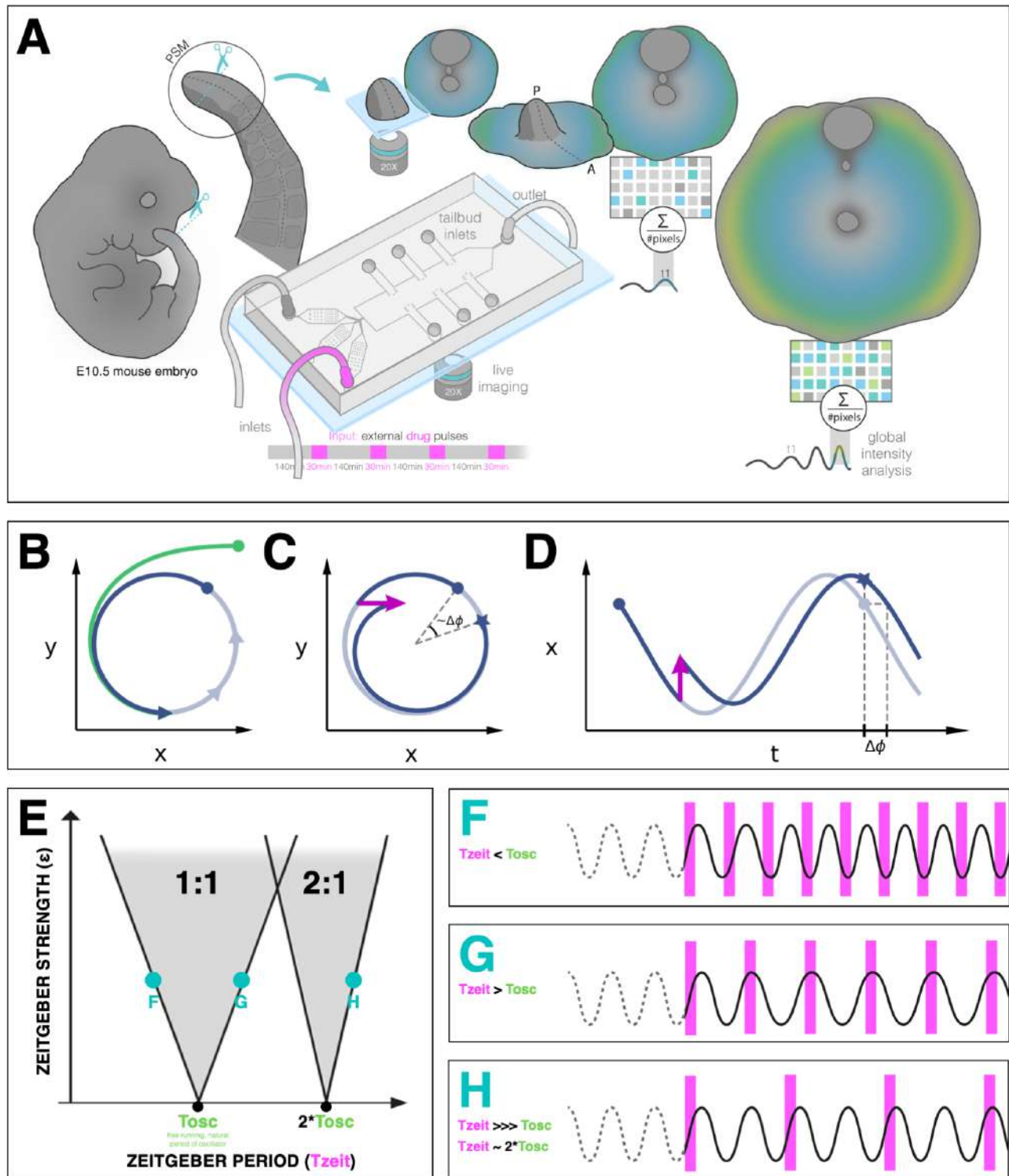


Fig. 1. Entrainment of an embryonic oscillator with a *zeitgeber*: setup and theory. (A) Schematic of the experimental entrainment setup using microfluidics device previously described in (1) and an overview of the coarse-graining approach used in this present study. A quasi- 2-dimensional segmentation assay, here simply referred to as 2D-assay, is used to quantify endogenous signaling oscillations in embryonic tissue expressing a dynamic fluorescent reporter (e.g. LuVeLu for Notch signaling), which is used as read-out for segmentation clock dynamics (approximated here as a single phase-oscillator). Simultaneously, the 2D-assay is subjected to periodic pulses of a drug (e.g. DAPT for Notch signaling), which serves as *zeitgeber*. Illustration by Stefano Vianello. A photo of the actual microfluidics device and its design are shown in Figure S1. (B) Abstract definition of phase: two different points in the plane (x, y) have the same phase if they converge on the same point on the limit cycle (indicated in grey). (C) Perturbations change the phase of the cycle by an increment $\Delta\phi$ (here phase is defined by the angle in the plane). (D) Time courses with similar perturbation as C showing the oscillations of x and phase difference $\Delta\phi$. (E) Illustration of generic Arnold tongues, plotted as a function of *zeitgeber* strength (ϵ) and *zeitgeber* period (T_{zeit}), mapping $n : m$ entrainment where the entrained oscillator (with natural period of T_{osc}) goes through n cycle/s for every m cycle/s of the *zeitgeber*. Three different points in the 1 : 1 and 2 : 1 Arnold tongues are specified with corresponding graphical illustration of an autonomous oscillator as it is subjected to *zeitgeber* with different periods (T_{zeit}): when T_{zeit} is less than T_{osc} (F), when T_{zeit} is greater than T_{osc} (G), and when T_{zeit} is much much greater than T_{osc} but is close to twice of T_{osc} (H). Free-running rhythm of the oscillator (i.e. before perturbation) is marked by a dashed line, while solid line illustrates its rhythm during perturbation with *zeitgeber*. Magenta bars represent the *zeitgeber* pulses. Illustration by Stefano Vianello.

84 Of note, an analogous oscillatory system was also described 141
85 during segmentation in arthropods (31) and while distinct at 142
86 molecular level, it also exhibits spatiotemporal wave patterns 143
87 traversing the embryo axis, again with indication of a period 144
88 gradient (32–35). 145

89 In this work, we coarse-grain these underlying complexities 146
90 and take a dynamical systems, macro-perspective on the seg- 147
91 mentation clock, studying it as a single phase-oscillator (Fig- 148
92 ure 1A). We build on the theory of synchronization and entrain- 149
93 ment (see below) to first perform a systematic experi- 150
94 mental characterization of its response to perturbation. We 151
95 compare the outcome to qualitative and quantitative theoret- 152
96 ical predictions. In turn, these experimental quantifications 153
97 allow to derive a phase response curve (PRC) that uniquely 154
98 characterizes the dynamical properties of the segmentation 155
99 clock. This new insight provides the means to understand- 156
100 and control- the timing of a complex embryological pattern-
101 ing process.

102 Theory of synchronization guides the experimental 158 103 study of segmentation clock entrainment. 159

104 Our experi- 160
105 mental study is based on and guided by the theory of entrain- 161
106 ment of oscillators by external periodic signal - a subset of 162
107 the general theory of synchronization (36). 163

108 Entrainment is observed when an autonomous oscillator 164
109 adapts its behaviour to lock to an external periodic signal 165
110 (called *zeitgeber* in the circadian rhythm literature). The 166
111 general theoretical framework to understand entrainment re- 167
112 quires the definition of oscillator phases (Figure 1B-D), and 168
113 their response to perturbation (37). Assuming the *zeitgeber* 169
114 consists in periodic pulses, entrainment is observed when the 170
115 phase of the oscillator ϕ_{ent} at the time of the *zeitgeber* is con- 171
116 stant (technically, a fixed point of the Poincaré return map 172
117 (38)). This defines period-locking (also termed mode lock- 173
118 ing) (36). 174

118 Entrainment is not always manifested and conditions for its 174
119 existence can be derived. Quantitatively, when entrainment 175
120 occurs, the *zeitgeber* induces a periodic phase perturbation 176
121 (or response) of the entrained oscillator, which *exactly* com- 177
122 pensates the detuning (or period mismatch, $T_{zeit} - T_{osc}$) be- 178
123 tween the *zeitgeber* and the free-running oscillator. For this 179
124 reason, when the detuning is very small, a weak external per- 180
125 turbation is enough to entrain an oscillator. Conversely, if 181
126 the detuning is big, a strong signal and associated response 182
127 is required for entrainment. One can then plot the minimal 183
128 strength of the *zeitgeber* (ϵ) versus corresponding detuning 184
129 (or simply T_{zeit} , if T_{osc} is constant): these maps are more 185
130 commonly known as Arnold tongues (Figure 1E). Arnold 186
131 tongues predict the period- and phase-locking behaviour in 187
132 oscillatory systems as different as electrical circuits (39), os- 188
133 cillatory chemical reactions (40–43), or living systems like 189
134 circadian rhythms (44). 190

135 Lastly, more complex patterns of entrainment can be ob- 190
136 served: for instance, stable phase relationships can be es- 191
137 tablished where the entrained oscillator goes through n cy- 192
138 cles for every m cycle of the external signal, defining $n : m$ 193
139 period-locking. In that case the instantaneous period of the 194
140 oscillator matches m/n the period of the *zeitgeber* (T_{zeit}). 195

Corresponding Arnold tongues can be obtained, leading to a rich structure for entrainment in parameter space (Figure 1F-H).

To experimentally apply the theory of synchronization to the segmentation clock, we make use of a microfluidics-based entrainment setup, which we had established previously in the lab (Figure S1) (1).

We showed before that using a quasi- 2-dimensional in vitro segmentation assay (hereafter referred to as a 2D-assay), which recapitulate segmentation clock dynamics and PSM patterning (27), the microfluidics-entrainment approach allowed us to take control of Notch and Wnt signaling oscillations, providing direct functional evidence that the oscillation phase shift between Wnt and Notch signaling is critical for PSM patterning (1).

156 Results

157 A coarse-grained, single oscillator description of the 158 159 segmentation clock. 160

161 To perform a systematic analysis of 162
163 entrainment dynamics, we decided to first introduce a coarse- 164
165 graining analysis strategy to quantify the rhythm of the seg- 166
167 mentation clock, without taking the spatial period differ- 168
169 ences, i.e. the period gradient along the AP axis, into account 170
171 (Figure 1A). To this end, the averaged signal intensity over 172
173 the entire sample was quantified. Our results show that this 174
175 approach indeed allows to quantitatively determine the peri- 176
177 od and phase of the signal averaged from the entire sample 178
179 (Figure 2). 180

181 Importantly, the oscillation period determined by using this 182
183 global analysis matched the periodic formation of morpho- 184
185 logical segment boundaries, as well as the period of Wnt sig- 186
187 nalling oscillations (i.e. Axin2) and the segmentation marker 188
189 Mesp2 (Figure 2C-F). Hence, we conclude that the global 189
190 time-series analysis provides a valid coarse-grained quantifi- 191
192 cation of the pace (period \sim rate of segment formation) and 193
194 rhythm (phase) of the segmentation clock. 195

196 The pace of the segmentation clock can be locked to a 197 198 wide range of entrainment periods. 199

200 Having established a 201
202 quantitative, coarse-grained read-out for segmentation clock 203
204 pace and rhythm, we next analyzed whether pace and rhythm 205
206 can be experimentally tuned using microfluidics-based en- 207
208 trainment (Figure 1A, S1). 209

210 First, we tested whether the segmentation clock can be en- 211
212 trained to periods different and far from the endogenous pe- 213
214 riod of ~ 140 mins, which we refer to as its free-running, nat- 215
216 ural period or T_{osc} . To address this question, we modified 216
217 the entrainment period from 120 to 180 minutes, while keep- 218
219 ing the drug concentration and the pulse duration (i.e. 30 219
220 mins/cycle) constant. Our results show that, while controls 220
221 cycled close to T_{osc} (Figure 3A-C, S2), the segmentation 221
222 clock rhythm in DAPT-entrained samples closely adjusted to 222
223 T_{zeit} over the specified range (Figure 3D, S2-S3). Hence, we 223
224 were able to speed up and slow down the pace of the segmen- 224
225 tation clock system using entrainment. 225

226 Notably, period-locking was less precise (i.e. higher standard 226
227 deviation as shown in Table S1) with 120-min and 180-min 227

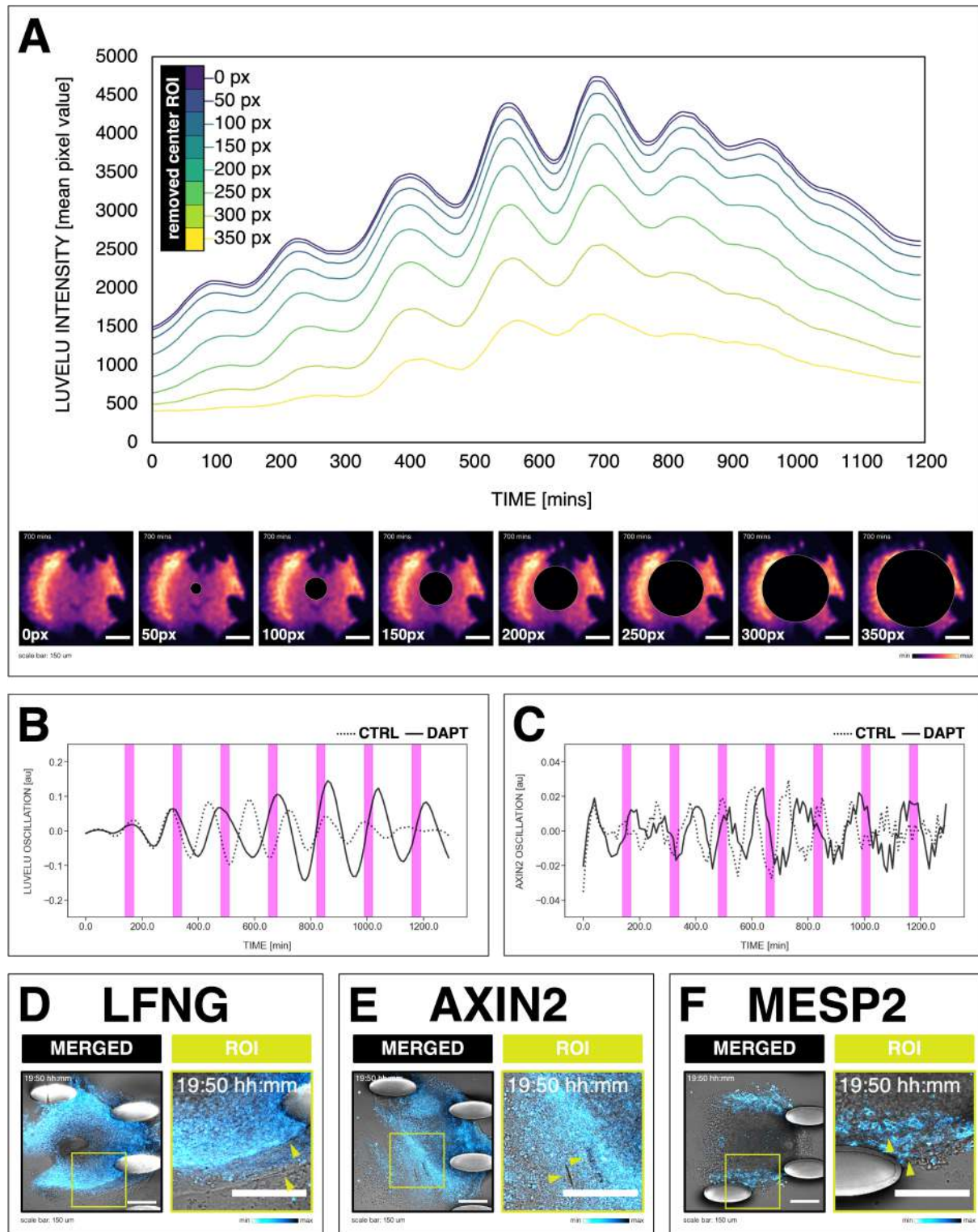


Fig. 2. Coarse-graining the segmentation clock using a global time-series analysis. (A) Comparison of measurements obtained from a region of interest (ROI) spanning either the entire field ("global ROI", 0 px) with ROIs, in which central regions of increasing size were excluded from quantification (excluded area specified in the top panel and marked with different colors). Bottom panel shows snapshot of signal of LuVeLU, a dynamic reporter of Notch signaling driven from the Lfng promoter (14), in a 2D-assay at 700 mins from the start of the experiment. Diameter of area excluded from the center is specified. A scheme of the experimental setup and the coarse-graining approach is illustrated in Figure 1A. The microfluidics device and its design are shown in Figures S1A and S1B, respectively. (B) Detrended timeseries of the segmentation clock (obtained using global ROI) in 2D-assays, which express the LuVeLU reporter, subjected to 170-min periodic pulses (magenta bars) of either 2 μ M DAPT (in solid line) or DMSO (for control, in dashed line). (C) Detrended timeseries of the segmentation clock (obtained using global ROI) in 2D-assays, which express the Axin2-linker-Achilles reporter, subjected to 170-min periodic pulses (magenta bars) of either 2 μ M DAPT (in solid line) or DMSO (for control, in dashed line). (D-F) Snapshot of 2D-assays, expressing either LuVeLU (D), Axin2-linker-Achilles (E), or Mesp2-GFP (F), and subjected to periodic pulses of 2 μ M DAPT, at 19:50 hh:mm (or 1190 mins) from the start of the experiment. Shown is the merge of the brightfield and the reporter channels. Also shown is a ROI in the merge of the two channels, with green arrowheads marking segment boundaries. Scale bar: 150 μ m.

196 *zeitgeber* periods, a possible indication that the limit of en- 252
197 trainment range is approached at these conditions.

198 We also tested the effect of changing *zeitgeber* strength (ϵ) on 253
199 entrainment dynamics. Synchronization theory predicts that 254
200 *zeitgeber* strength correlates with the time it takes to reach 255
201 period-locking (36, 45). To test this prediction, we entrained 256
202 samples with periodic DAPT pulses at fixed intervals of 170 257
203 minutes and varied drug concentration, in order to mimic 258
204 a change in *zeitgeber* strength (abbreviated with ϵ). We 259
205 indeed found that the time needed to show period-locking 260
206 was shortened in samples using higher DAPT concentrations 261
207 (Figure 4A-B, S4A). Additionally, as expected, higher drug 262
208 concentrations also resulted in more robust entrainment, 263
209 indicated by the quantifications of the first Kuramoto order 264
210 parameter, a measure for in-phase synchrony, between 265
211 samples (Figure 4C-D, 3A, S4B). 266

213 Higher-order entrainment of the segmentation clock. 268

214 In theory, a non-linear oscillator should be amenable not only 269
215 to 1 : 1 entrainment, but also to higher-order $n : m$ entrain- 270
216 ment, in which n cycles of the endogenous oscillation lock 271
217 to m cycles of the *zeitgeber* (36, 48). In practice, demon- 272
218 stration of higher-order entrainment is challenging due to the 273
219 narrow permissive parameter region, i.e. Arnold tongues are 274
220 progressively narrower away from the 1 : 1 regime. Strik- 275
221 ingly, we found experimental evidence for higher-order 2 : 1 276
222 entrainment (Figure 5). Samples entrained with either 300- 277
223 min (Figure 5A-B) or 350-min pulses showed evidence of 278
224 2 : 1 entrainment, i.e. the segmentation clock oscillated twice 279
225 per each *zeitgeber* pulse and hence the segmentation clock 280
226 rhythm adjusted to a period close to 175 minutes (Figure 281
227 5C). We confirmed that also during 2 : 1 entrainment, phase- 282
228 locking occurs. 283

229 The segmentation clock establishes a stable entrain- 284 230 ment phase relative to the *zeitgeber*. 285

231 We next analyzed the phase-locking behaviour between the segmen- 286
232 tation clock and the *zeitgeber*. According to dynamical systems theory, 287
233 phase-locking, i.e. the entrainment phase (ϕ_{ent}), can be char- 288
234 acterized as an attractor, i.e. it is a stable fixed point (38, 49). 289
235 To quantify the entrainment phase, we plotted the data as 290
236 stroboscopic maps (Figure 6A), which take a snapshot of the 291
237 segmentation clock phase at regular intervals based on *zeit-* 292
238 *geber* pulses (38, 49, 50). Stroboscopic maps enable determi- 293
239 nation of ϕ_{ent} as a stable fixed point that lies on the diagonal, 294
240 where there is phase-locking. 295

241 Plotting the stroboscopic maps shows that in samples en- 296
242 trained to periodic pulses of DAPT the segmentation clock 297
243 phase dynamics converge to a region on the diagonal, which 298
244 marks ϕ_{ent} (Figure 6B). Such convergence towards a stable 299
245 entrainment phase is further highlighted by looking at con- 300
246 secutive pulses and the corresponding phase trajectories of 301
247 individual samples. As exemplified in Figure 6C and as pre- 302
248 viously theoretically predicted (45, 51), at the same *zeitgeber* 303
249 strength and *zeitgeber* period, faster (or slower) convergence 304
250 towards this fixed point (i.e. entrainment) was achieved when 305
251 the initial phase of the endogenous oscillation (ϕ_{init}) was 306

closer (or farther) to ϕ_{ent} .

The phase of entrainment varies according to *zeitgeber* period. One fundamental property of entrained oscillatory systems is that its phase of entrainment varies as a function of the detuning, i.e. the period mismatch between endogenous oscillator and entrainment period (44, 52–55).

To test this theoretical prediction, we quantified ϕ_{ent} across a wide range of detuning, i.e. from 120-min to 180-min *zeitgeber* period. Indeed, we found that ϕ_{ent} , based on the centroid localization close to the diagonal in the stroboscopic maps, gradually changed its position as *zeitgeber* period, i.e. detuning, was varied (Figure 7A, S6). From 120-min to 180-min entrainment periods, ϕ_{ent} systematically shifted from $\sim\pi/2$ to $\sim3\pi/2$ (Figure 7A-B), spanning a range of almost π . Interestingly, theoretical studies have supported a "180-degree" rule (44), stating that the phase of entrainment varies by half a cycle (180° or π) within the range of permissible *zeitgeber* entrainment periods, T_{zeit} (44, 53). Hence, while at $T_{zeit} = 130$ mins the phase of entrainment was $2\pi/3 \pm \pi/6$, we found a phase of entrainment of $4\pi/3 \pm \pi/6$ at $T_{zeit} = 170$ mins. This means that the *zeitgeber* pulse coincides with the trough of the entrained segmentation clock at the former condition, while the *zeitgeber* pulse coincides with the clock's peak at the latter (Figure 7C). Hence, as predicted by theory, our results show that the segmentation clock phase of entrainment varies as a function of the detuning relative to *zeitgeber* pulses.

279 Phase response curves derivation and period change. 284

285 Building on our finding that the phase of entrainment varies 286
287 as a function of detuning (Figure 7B), our goal was to ex- 288
289 tract the quantitative information embedded in this dynamic 290
291 behaviour. This is possible since the phase of entrainment 292
293 dynamics reflect, at quantitative level, the fundamental prop- 294
295 erties of a dynamical system that responds to external pertur- 296
297 bations. This behaviour, in turn, can usually be captured with 298
299 a single function, the phase response curve (PRC) (44, 49). 300
301 The PRC describes the change of phase induced by a pertur- 302
303 bation, and a priori depends on both the nature of the pertur- 304
305 bation received and the phase of the cycle. Because of the 306
307 direct dependence of the phase of entrainment dynamics on 308
309 the PRC, our goal was to use the experimental data to gain 309
310 insight into the segmentation clock PRC.

To this end, and without loss of generality, we model perturbations in form of pulses of amplitude A and write :

$$\text{PRC}(\phi_{\text{pulse}}, A) = \phi_{\text{after pulse}}(\phi_{\text{pulse}}, A) - \phi_{\text{pulse}} \quad (1)$$

where ϕ_{pulse} is the phase of the segmentation clock *on the cycle* at the moment of the pulse, and $\phi_{\text{after pulse}}$ the phase after the pulse (which can be defined even if the system transiently moves outside of the limit cycle, via isochrons, see Winfree (56)). If, following a perturbation, the oscillator relaxes quickly towards the limit cycle, one can use the PRC to compute response to periodic pulses with period T_{zeit} . The sequence of phases at each pulse is then given by the strobo-

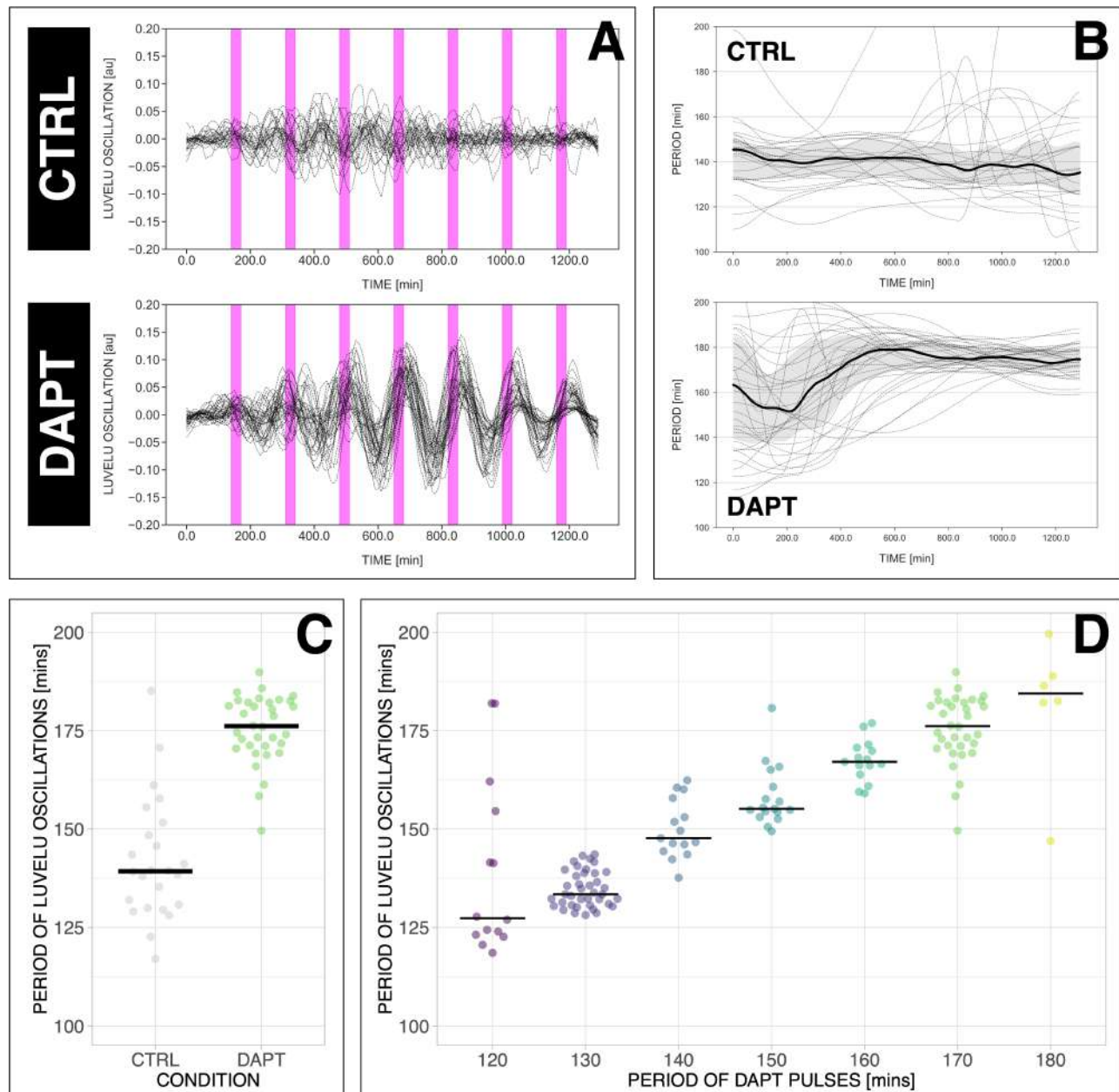


Fig. 3. The segmentation clock can be locked to a wide range of entrainment periods. (A) Detrended timeseries of the segmentation clock in 2D-assays subjected to 170-min periodic pulses of 2 μ M DAPT (or DMSO for controls). Periodic pulses are indicated as magenta bars and the timeseries of each sample (for CTRL: $n = 24$ and $N = 7$, for DAPT: $n = 34$ and $N = 8$) is marked with a dashed line. The gray shaded area corresponds to the interquartile range. (B) Period evolution during entrainment, obtained from wavelet analysis. The period evolution for each sample and the median of the periods are represented here as a dashed line and a solid line, respectively. The gray shaded area corresponds to the interquartile range. (C) Mean period from 650 to 850 mins after start of the experiment of samples subjected to 170-min periodic pulses of 2 μ M DAPT (or DMSO for controls). Each sample is represented as a dot, while the median of all samples is denoted as a solid horizontal line. (D) Mean period from 650 to 850 mins after start of the experiment of samples entrained to periodic pulses of 2 μ M DAPT. Each sample is represented as a dot, while the median of all samples is denoted as a solid horizontal line. The period of the DAPT pulses is specified (for 120-min: $n = 14$ and $N = 3$, for 130-min: $n = 39$ and $N = 10$, for 140-min: $n = 15$ and $N = 3$, for 150-min: $n = 17$ and $N = 4$, for 160-min: $n = 15$ and $N = 3$, for 170-min: $n = 34$ and $N = 8$, for 180-min: $n = 6$ and $N = 1$). Data were visualized using PlotsOfData (46), and a summary is provided in Table S1. A similar plot including each condition's respective control is in Figure S2. The analysis of period and wavelet power across time is summarized in Figure S3.

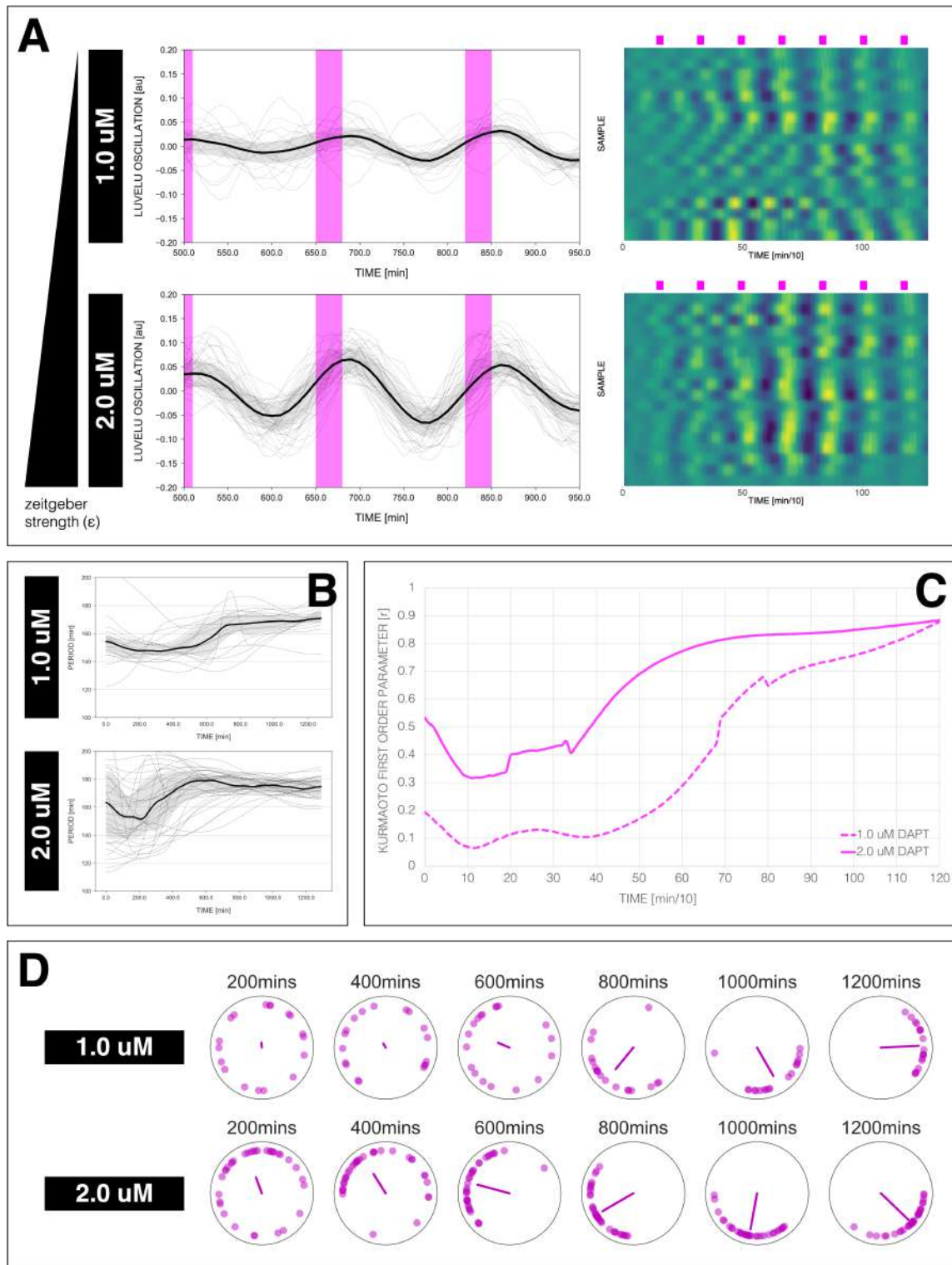


Fig. 4. Effect of varying DAPT concentrations on entrainment dynamics (A) Left: Detrended timeseries of the segmentation clock in 2D-assays entrained to 170-min periodic pulses of either 1.0 μM or 2.0 μM DAPT, zoomed in from 500 mins to 950 mins. Periodic pulses are indicated as magenta bars and the timeseries of each sample (for 1.0 μM : $n = 18$ and $N = 5$, for 2.0 μM : $n = 34$ and $N = 8$) is marked with a dashed line. The median of the oscillations is represented here as a solid line, while the gray shaded area denotes the interquartile range. Right: Detrended timeseries of the segmentation clock in 2D-assays entrained to 170-min periodic pulses of either 1.0 μM ($n = 18$ and $N = 5$) or 2.0 μM ($n = 18$ and $N = 8$) DAPT represented as heatmaps, generated using PlotTwist (47). Periodic pulses are indicated as magenta bars. Each row corresponds to a sample. **(B)** Period evolution during entrainment, obtained from wavelet analysis. The period evolution for each sample and the median of the periods are represented here as a dashed line and a solid line, respectively. The gray shaded area corresponds to the interquartile range. The plot for the 2.0 μM condition is the same as the plot for the DAPT condition in Figure 3B. **(C)** Evolution of first Kuramoto order parameter over time, showing change in coherence of multiple samples during the experiment. A first Kuramoto order parameter equal to 1.0 means that samples are in-phase. **(D)** Polar plots at different timepoints showing phase of each sample and their first Kuramoto order parameter, represented as a magenta dot along the circumference of a circle and a magenta line segment at the circle's center, respectively. A longer line segment corresponds to a higher first Kuramoto order parameter, and thus to more coherent samples. The direction of the line denotes the vectorial average of the sample phases. Time is indicated as mins elapsed from the start of the experiment.

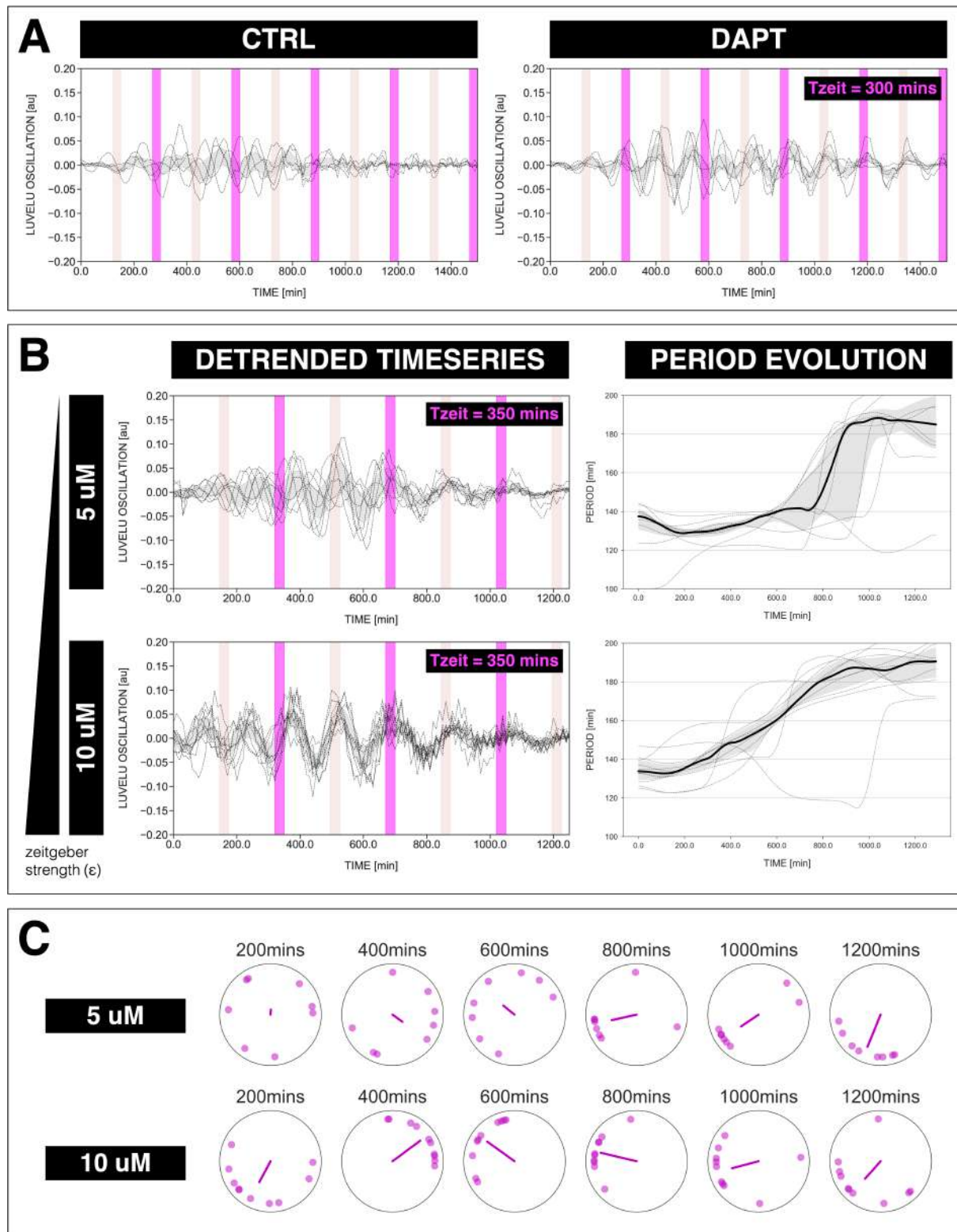


Fig. 5. The segmentation clock can be entrained to a higher order. (A) Detrended timeseries of the segmentation clock in 2D-assays subjected to 300-min periodic pulses of 2 μ M DAPT (or DMSO for controls). Periodic pulses are indicated as magenta bars and the timeseries of each sample (for CTRL: $n = 5$ and $N = 1$, for DAPT: $n = 5$ and $N = 1$) is marked with a dashed line. The gray shaded area denotes the interquartile range. Hypothetical pulses at half the *zeitgeber* period are indicated as light pink bars. (B) Left: Detrended timeseries of the segmentation clock in 2D-assays subjected to 350-min periodic pulses of either 5 μ M DAPT or 10 μ M DAPT. Periodic pulses are indicated as magenta bars and the timeseries of each sample (for 5 μ M DAPT: $n = 8$ and $N = 2$, for 10 μ M DAPT: $n = 10$ and $N = 2$) is marked with a dashed line. The gray shaded area denotes the interquartile range. Hypothetical pulses at half the *zeitgeber* period are indicated as light pink bars. Right: Period evolution during entrainment, obtained from wavelet analysis. The period evolution for each sample and the median of the periods are represented here as a dashed line and a solid line, respectively. The gray shaded area corresponds to the interquartile range. (C) Polar plots at different timepoints showing the phase of each sample in (B) and the first Kuramoto order parameter, represented as a magenta dot along the circumference of a circle and a magenta line segment at the circle's center, respectively. A longer line segment corresponds to a higher first Kuramoto order parameter, and thus to more coherent samples. The direction of the line denotes the vectorial average of the sample phases. Time is indicated as mins elapsed from the start of the experiment.

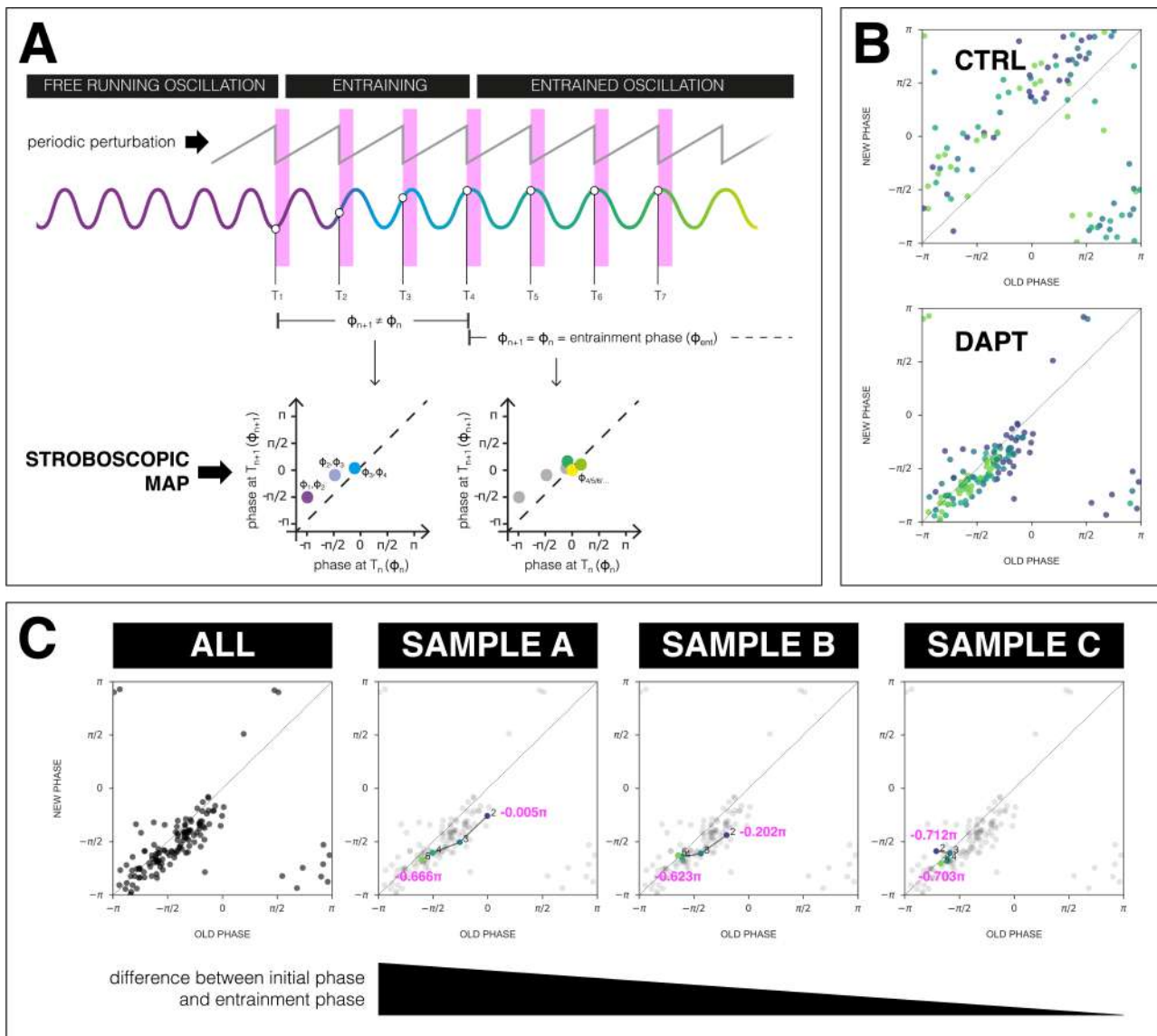


Fig. 6. The segmentation clock establishes a stable phase relationship with the zeitgeber. (A) Schematic of how to generate a stroboscopic map, where the phase of the segmentation clock just before a DAPT pulse (old phase, ϕ_n) is iteratively plotted against its phase just before the next pulse (new phase, ϕ_{n+1}). The position of each point in a stroboscopic map thus denotes a stepwise change in phase of the segmentation clock as it undergoes entrainment to the zeitgeber. Upon entrainment and phase-locking, the new phase is equal to the old phase lies on the diagonal of the stroboscopic map. This point on the diagonal is the entrainment phase (ϕ_{ent}). Illustration by Stefano Vianello. (B) Stroboscopic map of samples subjected to 170-min periodic pulses of 2 μ M DAPT (or DMSO for controls). Colors mark progression in time, from purple (early) to yellow (late). Note that while in control samples, points remain above the diagonal (reflecting that endogenous oscillations run faster than $T_{zeit} = 170$ mins as shown in Figure 3B-C), in entrained samples, the measurements converge towards a point on the diagonal (i.e. the entrainment phase, ϕ_{ent}), showing phase-locking. (C) Stroboscopic maps of the segmentation clock entrained to 170-min periodic pulses of 2 μ M DAPT ($n = 34$ and $N = 8$), for all samples (ALL) and for three individual samples (SAMPLE A, SAMPLE B, SAMPLE C). The numbers and colors (from purple to yellow) denote progression in time. The initial phase (old phase at point 2) and the entrainment phase (new phase at point 5) of each sample are specified.

304 stroboscopic map, introduced in Figure 6A:

$$\phi_{n+1} = (\phi_n + \text{PRC}(\phi_n, A) + T_{zeit}) \bmod T_{osc} \quad (2)$$

305 and 1 : 1 entrainment occurs when this stroboscopic map 316
306 converges towards a single fixed point ϕ_{ent} for a given 317
307 T_{zeit} . When T_{zeit} is varied, different phases of entrainment 318
308 $\phi_{ent}(T_{zeit})$ are observed, here plotted in (Fig. 7B).

309 To derive the PRC directly from the experimental strobo- 319
310 scopic maps, we invert Eq. 2 into :

$$\text{PRC}(\phi_n, A) = (\phi_{n+1} - \phi_n - T_{zeit}) \bmod T_{osc} \quad (3)$$

311 By estimating ϕ_n, ϕ_{n+1} for a given T_{zeit} , one can estimate 323
312 the PRC. The advantage of this approach is that it allows to 324

313 estimate PRC at any observed phase at the pulse ϕ_n , even
314 far from the entrainment phase ϕ_{ent} . Notice, however, that
315 phases far from ϕ_{ent} will be only sampled over the first few
pulses (so with possibly much noise) while conversely, ϕ_{ent}
will be quickly oversampled (and as such better defined statisti-
cally).

Figure 8A1 shows the PRC computed from the data as well
as Fourier series fits for different entrainment periods. PRCs
computed for different entrainment periods have a similar
shape, with similar locations for maxima and minima. Strik-
ingly, those PRCs are not sinusoidal but essentially 0 or
strongly negative, an unusual situation from a dynamical sys-

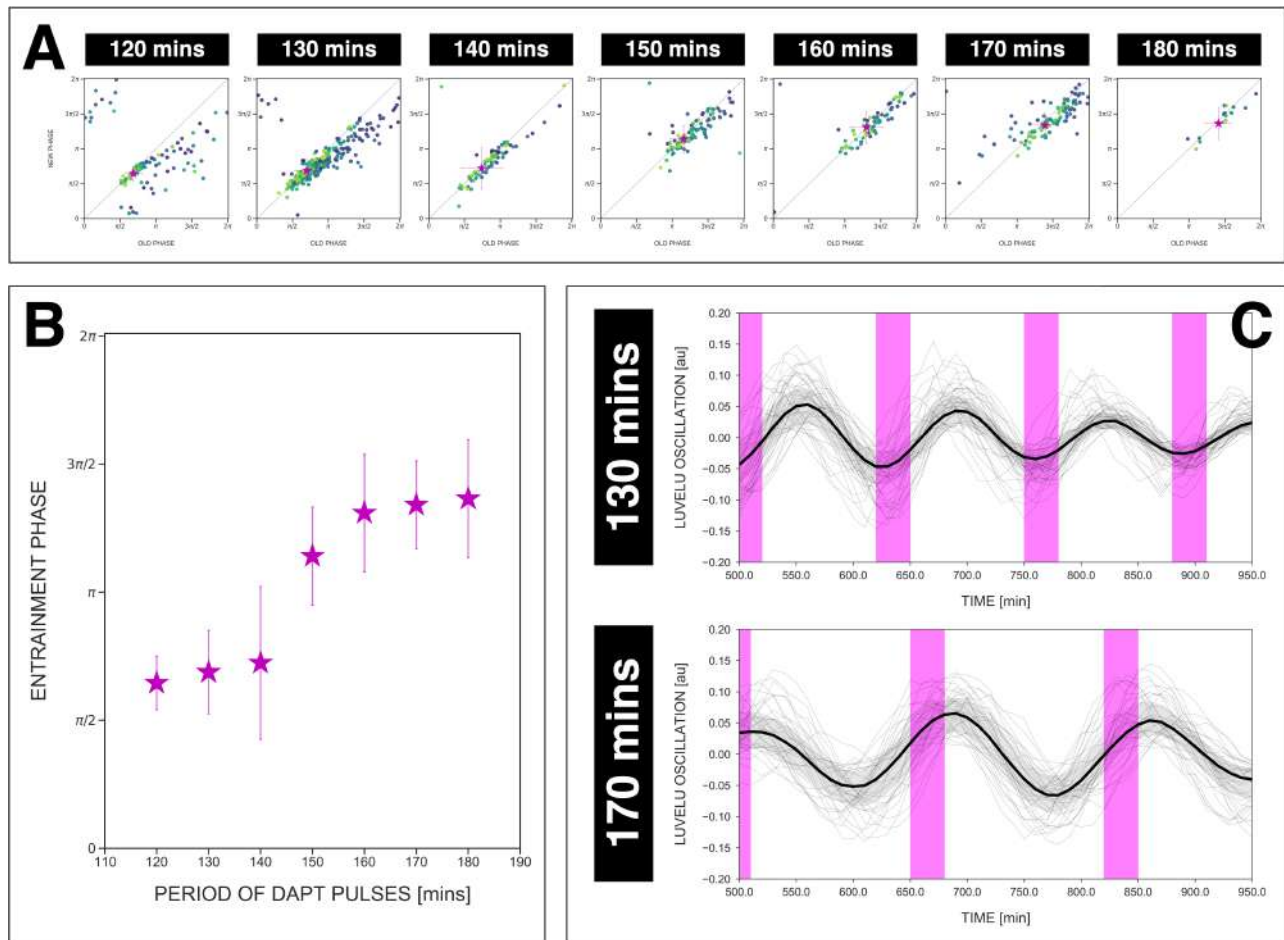


Fig. 7. The entrainment phase varies according to *zeitgeber* period within a range of π . (A) Stroboscopic maps for different periods of DAPT pulses (i.e. *zeitgeber* periods) placed next to each other. In these maps, only samples that were phase-locked by the end of the experiment are considered (for 120-min: $n = 13/14$ and $N = 3/3$, for 130-min: $n = 38/39$ and $N = 10/10$, for 140-min: $n = 10/15$ and $N = 3/3$, for 150-min: $n = 16/17$ and $N = 4/4$, for 160-min: $n = 11/15$ and $N = 3/3$, for 170-min: $n = 28/34$ and $N = 8/8$, for 180-min: $n = 4/6$ and $N = 1/1$). Here, a sample was considered phase-locked if the difference between its phase at the time of the final drug pulse considered and its phase one drug pulse before is less than $\pi/8$. The localized region close to the diagonal in each map marks the entrainment phase (ϕ_{ent}) for that *zeitgeber* period. This is highlighted with a magenta star, which corresponds to the centroid (x_c, y_c) . The centroid was calculated from the vectorial average of the phases of the samples at the end of the experiment, where $x_c =$ vectorial average of old phase, $y_c =$ vectorial average of new phase. The spread of the points in the region is reported in terms of the circular standard deviation ($\sqrt{-2 \ln R}$, where R is the first Kuramoto order parameter). The *zeitgeber* period is indicated above the maps. Colors mark progression in time, from purple to yellow. Stroboscopic maps of all samples and their respective controls are shown in Figure S6. Drug concentration and drug pulse duration were kept constant between experiments at 2 μ M and 30 mins/cycle, respectively. Phase 0 is defined as the peak of the oscillation. (B) Entrainment phase (ϕ_{ent}) at different *zeitgeber* periods, each calculated from the vectorial average of the phases of phase-locked samples at the time corresponding to last considered DAPT pulse. The spread of ϕ_{ent} between samples is reported in terms of the circular standard deviation ($\sqrt{-2 \ln R}$, where R is the first Kuramoto order parameter). (C) Detrended timeseries of the segmentation clock in 2D-assays entrained to either 130-min or 170-min periodic pulses of 2 μ M DAPT, zoomed in from 500 mins to 950 mins. Periodic pulses are indicated as magenta bars and the timeseries of each sample (for 130-min: $n = 39$ and $N = 10$, for 170-min: $n = 34$ and $N = 8$) is marked with a dashed line. The median of the oscillations is represented here as a solid line, while the gray shaded area denotes the interquartile range. The full detrended timeseries for the 170-min condition can be seen in Figure 3A.

tems theory standpoint associated to special classes of oscillators (see more details below and in Discussion). However, contrary to theoretical predictions, the inferred PRCs at different entrainment periods do not overlap and appear shifted vertically as T_{zeit} is changed.

Such vertical shifts in PRCs as a function of entrainment period have been previously observed in so-called “overdrive suppression” for cardiac cell oscillators (57). Shifts occur when the entrainment signal impacts the biochemical control of the system, leading to a change of intrinsic period (here T_{osc}). Here, such change of intrinsic period can not be directly measured experimentally, as the system is entrained to another period, however, we found several lines of experimental and theoretical evidence, in addition to the vertical

PRC shift, in full agreement with such an effect.

First, the slope of the $\phi_{ent}(T_{zeit})$ curve in Figure 7B is unusual: PRC theory predicts that for high and low detuning this curve should have vertical slopes. Here, we observed plateaus in the data, which can be simply explained if the intrinsic period changes (see mathematical explanation in Supplementary Note 2). In addition, we performed entrainment release experiments, where the segmentation clock is first entrained, then released (Figure S5): we observed a slow recovery over several cycles to a period matching control samples, compatible with a transient change of the intrinsic period. This effect was confirmed by a more precise study of the phase return map after release (Figure S5B). Combined, the inference of the PRC based on entrainment quantifica-

353 tion data thus reveals two properties- a highly asymmetrical, 410 strategy.
354 mainly negative PRC and second, a change of intrinsic period
355 during entrainment.

356 **ERICA model and Arnold tongue.** To gain understanding 412
357 of these findings from a theory perspective, we next build a 413
358 minimal model of our data. 414

359 First, we take the PRC computed at $T_{zeit} = 140$ mins to be 415
360 the "reference" period, since it coincides with the natural pe- 416
361 riod of the process. We can then estimate for each entrain- 417
362 ment period the period shift most consistent with the data, 418
363 to obtain a single, period independent PRC in Figure 8A2

364 (see Supplementary Note 2). From there, we build upon the 419
365 simplest non-linear phase-oscillator, i.e. the classical Radial 420
366 Isochron Cycle (RIC). To modulate its sine-form PRC, which 421
367 is incompatible with our data, we perturb it into an Elliptic 422
368 Radial Isochron Cycle with Acceleration or ERICA. 423

369 ERICA is designed to have radial isochrons, meaning that 424
370 the phase (and the PRC) can be analytically computed in the 425
371 entire plane. ERICA then allows for the speeding up of the 426
372 cycle for some angle range (parameter s_*) or for changes of 427
373 the limit cycle shape into an ellipse of increasing eccentric- 428
374 ity (parameter λ). Both high values of λ and s_* generate high 429
375 negative asymmetry in the PRC (see Supplement; the full jus- 430
376 tification of the ERICA construction, the study of its multi- 431
377 ple properties and its connection to biological oscillators will 432
378 be described elsewhere). We then used Monte Carlo (MC) 433
379 optimization to find parameters best fitting the experimental 434
380 PRC. The results from this MC optimization put the oscilla- 435
381 tor far from the standard RIC oscillator (see cycle and cor- 436
382 responding flow in Figure 8B), consistent with strongly neg- 437
383 ative PRCs, with a moderate value of perturbation $A = 0.4$, 438
384 high value of $\lambda = 0.5$ (indicating a strong elliptical shape), 439
385 and high value of $s_* = 5.6$ over half a cycle (indicative of 440
386 excitability). Figure 8C compares the PRC of this optimized 441
387 model with the multiple data points, showing excellent agree- 442
388 ment. In addition, we combined the ERICA framework with 443
389 a simple fit for intrinsic period change to account for the ex- 444
390 perimental phase transition curves, as illustrated in Figure 445
391 8G. 446

392 With the ERICA model at hand, we derived numerically the
393 Arnold tongues of the system and the phase/detuning curves 447
394 for all entrainment parameters (Figure 8E-F). We notice that 448
395 the Arnold tongues are heavily skewed toward the right, 449
396 meaning that the system can be more easily slowed down 450
397 than sped-up, consistent with the negative PRC shape. Re- 451
398 markably, while we build the model using only one entrain- 452
399 ment drug concentration, we can also largely explain data ob- 453
400 tained at other concentrations (Figure 8F). In particular, the 454
401 Arnold tongues/our model predict a specific change of the 455
402 entrainment phase as the entrainment strength is varied (Fig- 456
403 ure S12G). The comparison to experimental data (Figure S7) 457
404 shows this prediction is, qualitatively, verified. More gener- 458
405 ally, having the PRC and a minimal, coarse-grained model 459
406 that captures the essential dynamical features of the segmen- 460
407 tation clock during entrainment, including the change in in- 461
408 trinsic period, enables predictable control over the pace and 462
409 the rhythm of the segmentation clock using the entrainment 463

411 Discussion

In this work, we used a coarse-graining, entrainment ap-
proach to gain new insights into the dynamic properties of
the segmentation clock from dynamical systems perspective.
We mode-lock the segmentation clock to various entrainment
periods and use the information about the dynamic phase-
locking behaviour to derive the somite segmentation clock
phase-response curve from the experimental data.

A coarse-graining approach captures essential dynamical features using a simple "one oscillator" phase description.

Given the complexity underlying the somite segmentation clock, comprised of several, interconnected, signaling pathways with countless molecular interactions, it was a priori unclear whether a simple "one oscillator" phase description and perturbation approach would capture the essential dynamical characteristics at the systems level. Another potential difficulty arises from the fact that cellular oscillators define a phase gradient, controlling the segmentation pattern (27). For all those reasons, one could imagine that no single phase could describe the systems behaviour, a general concern for systems of interacting oscillators already mentioned by Winfree (56).

Remarkably, one key finding of this work is that indeed, using a systems-level single oscillator phase description, we observe a consistent entrainment behaviour, i.e. period-locking with convergence towards a well-defined entrainment phase, as predicted from the oscillator phase response theory. It is important to point out that theoretical predictions are non-trivial and quantitative, such as the higher order 2 : 1 entrainment (Figure 5) and the dependence of the entrainment phase on detuning (Figure 7A-B). Given these experimental findings we conclude that the coarse-graining approach and the description of the entire system using a single oscillator phase is justified and enables to extract the essential dynamical properties, which are captured by a mathematical model including the systems' PRC.

Asymmetrical segmentation clock PRC compatible with saddle-node on invariant cycle (SNIC) bifurcation.

Insight into the systems' PRC allows to infer about the nature and characteristics of the oscillatory system, independent of its specific molecular realization (49). For instance, excitable systems can be functionally categorized with their PRC, i.e. in neuroscience, systems where the period of action potential is tunable with some input current are called Class I excitable systems, and have PRCs with constant sign. (49). Such highly asymmetrical PRC can be contrasted with systems with sinusoidal PRC, in which the period is not tunable. Such PRCs are observed in biological systems such as the circadian clocks (51), and associated to Kuramoto coupling (37).

The Segmentation Clock PRC that we computed here rather shares features with Class I excitable systems, consistent with a recent theoretical proposal (58). Those oscillators are close

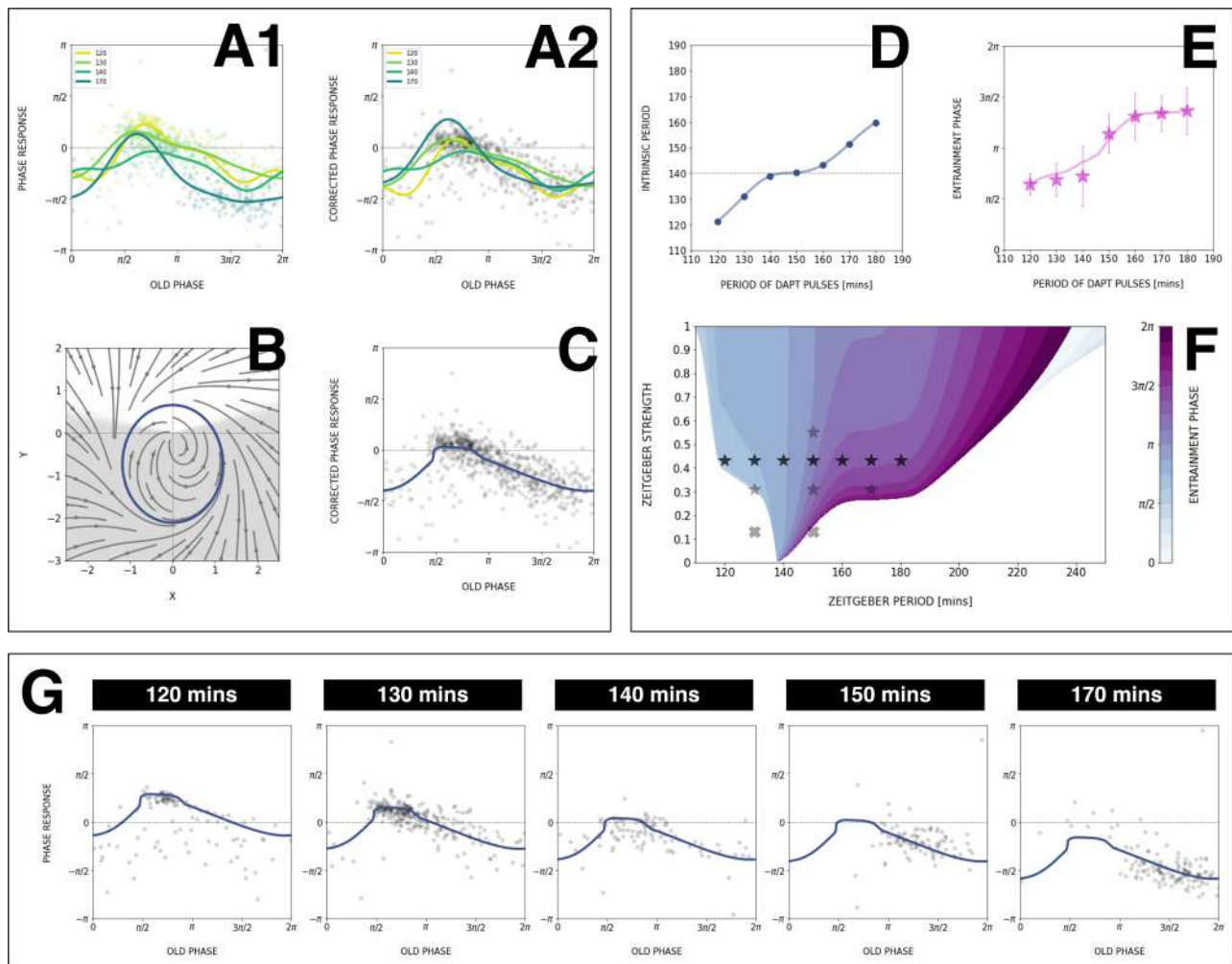


Fig. 8. Modelling segmentation clock entrainment response. (A) PRC from the data for different *zeitgeber* periods. (1) PRCs calculated at different T_{zeit} (points) and Fourier series fitted to them (lines). (2) Original PRCs are shifted vertically to collapse the data points on one curve. (B) Oscillator model, optimized by fitting the vertically shifted PRC. The limit cycle is an ellipse (blue) with eccentricity $\lambda = 0.5$, the region with speeding up $s_* = 5.6$ is shaded. (C) Optimized model PRC (line) overlaid to the vertically shifted data points. (D) Modelled intrinsic period T_{osc} as a function of entrainment period T_{zeit} . Points were inferred from the PRCs data in A1 by matching the detuning and entrainment phase ϕ_{ent} , the function was interpolated with cubic splines. (E) Entrainment phase ϕ_{ent} from the model with changing intrinsic period (line) agrees with the experimental data (points and error bars). (F) 1 : 1 Arnold tongue and isophases calculated with the model. Stars correspond to experimental data (T_{zeit} , A) with observed entrainment, in agreement with ϕ_{ent} data for different DAPT concentrations (Figure S7A). Black stars represent the experiments used for optimizing the model. Crosses correspond to experimental conditions with no entrainment. (G) Fit of the model (solid lines) overlaid with experimental phase differences (dots) at different periods T_{zeit} .

464 to a saddle-node on invariant cycle (SNIC) bifurcation and 482
 465 show a period that can be arbitrarily long depending on the 483
 466 proximity to the bifurcation. Interestingly, the segmenta- 484
 467 tion clock does show slowing down behaviour at multiple 485
 468 levels before oscillations halt: at cellular level, PSM cells
 469 slow down their oscillatory activity as they progress towards 486
 470 differentiation and eventually stop oscillations. In addition, 487
 471 at the systems level analyzed here, the segmentation clock 488
 472 slows down over developmental time, too, a feature described 489
 473 in several species. Combined with the mostly negative PRCs 490
 474 that we obtained for the segmentation clock, we conclude that 491
 475 the system has a natural bias of slowing down the oscillations, 492
 476 reflected in its PRC and reminiscent of oscillators close to 493
 477 SNIC bifurcation/ Class I excitability. 494
 478 SNIC appear naturally when the regulatory logic of a system 495
 479 moves from a negative feedback oscillator to multistability 496
 480 (58), thus reflecting underlying network modularity. Such 497
 481 modularity and robustness with changes in regulatory logic 498

is a hallmark of developmental plasticity (59) and hence one
 would anticipate to find SNIC oscillators to be abundant in
 developing systems. First examples are indeed emerging,
 such as during *C. elegans* development (60).

Findings not predicted by the theory of PRC. We also
 made several unexpected findings, not predicted by the theory
 of PRC.

First, we found evidence that during entrainment, not only
 does the segmentation clock adjust its observed period to the
zeitgeber pulses, but also, changes its intrinsic period in the
 direction of the *zeitgeber* rhythm. Hence, during entrainment
 that slows down the clock (i.e. 170 mins), we find evidence
 that the intrinsic period lengthens (not just the observed
 rhythm), while during entrainment that speeds up the clock
 (i.e. 120 mins), we find evidence that the intrinsic period
 decreased. Again, such a changes of intrinsic period is
 not predicted in entrained systems. The simplest explanation

could be that the drug pulses change the period of the oscillator by changing some biochemical parameter in the system, similar to overdrive suppression in cardiac cells (57). However, as stated above, we do not find evidence for a consistent slowing down or speeding up effect: the intrinsic period is decreased for short entrainment cycles and increased for longer entrainment cycles. This rather suggests the existence of feedbacks of the clock on itself, leading to higher order adaptations beyond the rapid Notch phase response. One can only speculate on the mechanisms underlying such adaptation, but this is compatible with the idea that two interacting oscillators control the intrinsic period. Here, it is possible that entraining Notch with a *zeitgeber* modifies the Wnt oscillation period, which in turn feeds back on Notch on a longer time scale. So the internal period change that we see might in fact come from the induced change of Wnt period. We have shown previously Wnt and Notch oscillators are coupled but are not phase-locked, with functional impact on tissue patterning (1). Alternatively, a similar role could also be played by the long inter or intracellular delays in the system, postulated in multiple theoretical works (25, 61, 62). Such delays could effectively couple multiple cycles, changing clock parameters (such as the period) beyond instantaneous phase response. More experimental and theoretical work is needed to explore these ideas.

Second, a striking outcome we obtained was that even after entrainment, the system exhibited a spatial period gradient and phase waves (Figure S8). Put differently, while the overall system is entrained, as evidenced by a control of the timing of morphological segmentation and of segmentation clock rhythm, the underlying cellular oscillators show a divergent, yet, structured response, i.e. a period gradient is visible. How the macro-scale behaviour relates to the underlying cellular scale oscillations needs to be further explored in follow up studies investigating the role of intra- and intercellular coupling underlying the entrainment response.

Conclusions

Our work demonstrates how, despite all the molecular and functional complexities, coarse-graining and theory can be used to effectively take control of complex biological processes. A *molecular* mechanism is not needed to exert control, as long as we have a *mathematical* one, one, that captures the essential features of a system at a meaningful coarse-grained level.

We also aim to illustrate the potential of an integrated, theoretical-experimental approach to complex biological systems: while from theoretical viewpoint, the fact that entrainment phase varies as detuning is altered is a mathematical necessity and hence 'obvious', this outcome is not at all intuitive, *a priori*, from an experimental-observational viewpoint. Theory guides experimentation, i.e. Figure 1 Theory, leading to new insight and understanding of a complex biological phenomenon.

Additional studies are needed to gain further insight into the response to other perturbation regimes, importantly at both the systems-level and also at cellular-scale. We consider that

such a dynamical systems theoretical-experimental approach is a promising and, as we show here, feasible way forward with the goal to categorize the segmentation clock in its universality class.

Materials and methods

Please refer to supplementary materials (Supplementary Note 1) for detailed materials and methods.

ACKNOWLEDGEMENTS

We thank Mogens Høgh Jensen, Jonas Juul, Mathias Heltberg, Sandeep Krishna, Adrián Granada and Istvan Kiss for in depth discussions on Arnold tongues and PRC; Justin Crocker, Anne Ephrussi, Lars Hufnagel, Jelle Scholtalbers, Ulrich Schwarz, Stefano Vianello, Nachiket Satish Shembekar and Ramesh Utharala, and all the members of the Aulehla group for the discussions and feedback. We are very grateful to Stefano Vianello for also designing some of the figures. We thank Antonio Politi for providing the Pipeline Constructor macro for automated live microscopy. We also acknowledge the assistance from Maximilian Beckers, Aliaksandr Halavatyi, and Oleksandr Maistrenko in writing scripts for data analysis. We are thankful to Ricardo Henriques for kindly sharing the template that was used to format this preprint. Following EMBL core facilities are acknowledged for their support of this work: the EMBL Advanced Light Microscopy Facility (ALMF), the EMBL Laboratory Animal Resources (LAR), the EMBL Mechanical Design Office and the EMBL Mechanical Workshop. The work was supported by the European Molecular Biology Laboratory (EMBL), by the German Research Foundation/DFG (CRC/SFB 1324, project number 331351713) to AA, the National Research Council of Canada, Discovery Grant program to Paul François, by the New Frontiers in Research Fund, Exploration program to PF and AA and the European Research Council (ERC) via an ERC Starting Grant (agreement n. 633943) and Consolidator Grant (agreement n.n.866537) to Alexander Aulehla.

AUTHOR CONTRIBUTIONS

Paul Gerald Layague Sanchez designed the project, made the microfluidics devices, performed experiments, analyzed the data, and wrote the manuscript. Victoria Mochulska extracted PRCs, designed and optimized the ERICA model, and performed simulations. Christian Mauffette Denis optimized the model and performed Arnold tongue simulations. Katharina Sonnen developed the microfluidics-based experimental platform, performed experiments and contributed to the project design. Takehito Tomita quantified and analyzed the period gradient. Gregor Mönke contributed to the project design and developed the wavelet analysis workflow used for the quantification of experimental time series. Nobuko Tsuchida-Straeten and Yvonne Petersen generated the Axin2-linker-Achilles mouse line. Paul François designed the ERICA model, supervised the theory part of the project and wrote the manuscript. Alexander Aulehla designed and supervised the project and wrote the manuscript.

COMPETING FINANCIAL INTERESTS

The authors declare no competing financial interests.

Bibliography

1. Katharina F Sonnen, Volker M Lauschke, Julia Uraji, Henning J Falk, Yvonne Petersen, Maja C Funk, Mathias Beaupeux, Paul François, Christoph A Merten, and Alexander Aulehla. Modulation of phase shift between wnt and notch signaling oscillations controls mesoderm segmentation. *172(5):1079–1090.e12*, 2018. ISSN 0092-8674. doi: 10.1016/j.cell.2018.01.026.
2. David Marr and Tomaso Poggio. From understanding computation to understanding neural circuitry. *dspace.mit.edu*, 1976.
3. John Cardy. *Scaling and renormalization in statistical physics*, volume 5. Cambridge university press, 1996. doi: 10.1017/CBO9781316036440.
4. William Bialek. Perspectives on theory at the interface of physics and biology. 2015.
5. Benjamin B Machta, Ricky Chachra, Mark K Transtrum, and James P Sethna. Parameter space compression underlies emergent theories and predictive models. *Science*, 342(6158):604–607, 2013.
6. Félix Proulx-Girardeau, Thomas J Rademaker, and Paul François. Untangling the hairball: Fitness-based asymptotic reduction of biological networks. *Biophysical Journal*, 113(8):1893–1906, 2017.
7. CJ Hsu, GJ Brouhard, and P François. Numerical parameter space compression and its application to biophysical models. *Biophys J*, 118(6):1455–1465, 2020.
8. Isabel Palmeirim, Domingos Henrique, Ish-Horowitz, David, and Olivier Pourquié. Avian hairy gene expression identifies a molecular clock linked to vertebrate segmentation and somitogenesis. *91(5):639–48*, 1997. ISSN 0092-8674. doi: 10.1016/S0092-8674(00)80451-1.
9. Aurélie J Krol, Daniela Roellig, Mary-Lee Dequéant, Olivier Tassy, Earl Glynn, Gaye Hattem, Arcady Mushegian, Andrew C Oates, and Olivier Pourquié. Evolutionary plasticity of segmentation clock networks. *Development*, 138(13):2783–2792, 2011. doi: 10.1242/dev.063834.
10. Mary-Lee Dequéant and Olivier Pourquié. Segmental patterning of the vertebrate embryonic axis. *9(5):370–382*, 2008. ISSN 1471-0056. doi: 10.1038/nrg2320.
11. Alexis Hubaud and Olivier Pourquié. Signalling dynamics in vertebrate segmentation. *15(11):709–721*, 2014. ISSN 1471-0072. doi: 10.1038/nrm3891.

- 630 12. Alexander Aulehla, Christian Wehrle, Brand-Saber, Beate, Rolf Kemler, Achim Gossler, 716
631 Benoit Kanzler, and Bernhard G Herrmann. Wnt3a plays a major role in the segmentation 717
632 clock controlling somitogenesis. 4(3):395–406, 2003. ISSN 1534-5807. doi: 10.1016/j.
633 S1534-5807(03)00055-8. 719
- 634 13. Mary-Lee Dequ ant, Earl Glynn, Karin Gaudenz, Matthias Wahl, Jie Chen, Arcady Mushe- 720
635 gian, and Olivier Pourqu . A complex oscillating network of signaling genes underlies 721
636 the mouse segmentation clock. 314(5805):1595–1598, 2006. ISSN 0036-8075. doi: 722
637 10.1126/science.1133141. 723
- 638 14. Alexander Aulehla, Winfried Wiegraebe, Valerie Baubet, Matthias B Wahl, Chuxia Deng, 724
639 Makoto Taketo, Mark Lewandoski, and Olivier Pourqu . A β -catenin gradient links the clock 725
640 and wavefront systems in mouse embryo segmentation. 10(2):186–93, 2007. ISSN 1465- 726
641 7392. doi: 10.1038/ncb1679. 727
- 642 15. Li-Fang Chu, Daniel Mamott, Zijian Ni, Rhonda Bacher, Cathy Liu, Scott Swanson, Christina 728
643 Kendzioriski, Ron Stewart, and James A Thomsson. An in vitro human segmentation clock 729
644 model derived from embryonic stem cells. *Cell reports*, 28(9):2247–2255, 2019. doi: 10.730
645 1016/j.celrep.2019.07.090. 731
- 646 16. Margarete Diaz-Cuadros, Daniel E Wagner, Christoph Budjan, Alexis Hubaud, Oscar A 732
647 Tarazona, Sophia Donnelly, Arthur Michaut, Ziad Al Tanoury, Kumiko Yoshioka-Kobayashi, 733
648 Yusuke Niino, et al. In vitro characterization of the human segmentation clock. *Nature*, 580 734
649 (7801):113–118, 2020. doi: 10.1038/s41586-019-1885-9. 735
- 650 17. Mitsuhiro Matsuda, Yoshihiro Yamanaka, Maya Uemura, Mitsujiro Osawa, Megumu K Saito, 736
651 Ayako Nagahashi, Megumi Nishio, Long Guo, Shiro Ikegawa, Satoko Sakurai, et al. Re- 737
652 capitulating the human segmentation clock with pluripotent stem cells. *Nature*, 580(7801): 738
653 124–129, 2020. doi: 10.1038/s41586-020-2144-9. 739
- 654 18. Miquel Maroto, Kim J Dale, Mary-Lee Dequ ant, Anne-C cile Petit, and Olivier Pourqu . 740
655 Synchronised cycling gene oscillations in presomitic mesoderm cells require cell-cell con- 741
656 tact. 49(2-3):309–15, 2005. ISSN 0214-6282. doi: 10.1387/jjdb.041958mm. 742
- 657 19. Yoshito Masamizu, Toshiyuki Ohtsuka, Yoshiki Takashima, Hiroki Nagahara, Yoshiko Take- 743
658 naka, Kenichi Yoshikawa, Hitoshi Okamura, and Ryoichiro Kageyama. Real-time imaging of 744
659 the somitic segmentation clock: revelation of unstable oscillators in the individual presomitic 745
660 mesoderm cells. 103(5):1313–8, 2006. ISSN 0027-8424. doi: 10.1073/pnas.0508658103. 746
- 661 20. Leah Herrgen, Sa l Ares, Luis G Morelli, Christian Schr ter, Frank J licher, and Andrew C 747
662 Oates. Intercellular coupling regulates the period of the segmentation clock. 20(14):1244– 748
663 1253, 2010. ISSN 0960-9822. doi: 10.1016/j.cub.2010.06.034. 749
- 664 21. Alexis B Webb, Iv n M Lengyel, David J J rg, Guillaume Valentin, Frank J licher, Luis G 750
665 Morelli, and Andrew C Oates. Persistence, period and precision of autonomous cellular 751
666 oscillators from the zebrafish segmentation clock. 5:e08438, 2016. doi: 10.7554/eLife. 752
667 08438. 753
- 668 22. Kumiko Yoshioka-Kobayashi, Marina Matsumiya, Yusuke Niino, Akihiro Isomura, Hiroshi 754
669 Kori, Atsushi Miyawaki, and Ryoichiro Kageyama. Coupling delay controls synchronized 755
670 oscillation in the segmentation clock. *Nature*, 580(7801):119–123, 2020. doi: 10.1038/ 756
671 s41586-019-1882-z. 757
- 672 23. Laurel A Rohde, Arianne Bercowsky-Rama, Jose Negrete, Guillaume Valentin, Sundar Ram 758
673 Naganathan, Ravi A Desai, Petr Strnad, Daniele Soroldoni, Frank J licher, and Andrew C 759
674 Oates. Cell-autonomous generation of the wave pattern within the vertebrate segmentation 760
675 clock. *bioRxiv*, 2021. doi: 10.1101/2021.05.29.446196. 761
- 676 24. C line Gomez, Ertu rl  zbudak, Joshua Wunderlich, Diana Baumann, Julian Lewis, and 762
677 Olivier Pourqu . Control of segment number in vertebrate embryos. *Nature*, 454(7202): 763
678 335, 2008. ISSN 1476-4687. doi: 10.1038/nature07020. 764
- 679 25. Luis G Morelli, Sa l Ares, Leah Herrgen, Christian Schr ter, Frank J licher, and Andrew C 765
680 Oates. Delayed coupling theory of vertebrate segmentation. 3(1):55–66, 2009. ISSN 1955- 766
681 2068. doi: 10.2976/1.3027088. 767
- 682 26. Andrew C Oates, Luis G Morelli, and Sa l Ares. Patterning embryos with oscillations: struc- 768
683 ture, function and dynamics of the vertebrate segmentation clock. 139(4):625–639, 2012. 769
684 ISSN 0950-1991. doi: 10.1242/dev.063735. 770
- 685 27. Volker M Lauschke, Charisios D Tsiarlis, Paul Fran ois, and Alexander Aulehla. Scaling 771
686 17 of embryonic patterning based on phase-gradient encoding. 493(7430):101, 2012. ISSN 772
687 1476-4687. doi: 10.1038/nature11804. 773
- 688 28. Daniele Soroldoni, David J J rg, Luis G Morelli, David L Richmond, Johannes Schindelin, 774
689 Frank J licher, and Andrew C Oates. A doppler effect in embryonic pattern formation. 345 775
690 (6193):222–225, 2014. ISSN 0036-8075. doi: 10.1126/science.1253089. 776
- 691 29. Charisios D Tsiarlis and Alexander Aulehla. Self-Organization of embryonic genetic oscil- 777
692 lators into spatiotemporal wave patterns. 164(4):656–667, 2016. ISSN 0092-8674. doi: 778
693 10.1016/j.cell.2016.01.028. 779
- 694 30. Henning Johannes Falk. *Imaging the onset of the segmentation clock during mouse gas- 780*
695 *trulation*. PhD thesis, 2019. 781
- 696 31. Erik Clark, Andrew D Peel, and Michael Akam. Arthropod segmentation. *Development*, 146 782
697 (18):dev170480, 2019. doi: 10.1242/dev.170480. 783
- 698 32. Andres F Sarrazin, Andrew D Peel, and Michalis Averof. A segmentation clock with two- 784
699 segment periodicity in insects. *Science*, 336(6079):338–341, 2012. doi: 10.1126/science. 785
700 1218256. 786
- 701 33. Ezzat El-Sherif, Michalis Averof, and Susan J Brown. A segmentation clock operating in 787
702 blastoderm and germband stages of tribolium development. *Development*, 139(23):4341– 788
703 4346, 2012. doi: 10.1242/dev.085126. 789
- 704 34. Carlo Brena and Michael Akam. An analysis of segmentation dynamics throughout em- 790
705 bryogenesis in the centipede strigamia maritima. *BMC biology*, 11(1):1–18, 2013. doi: 791
706 10.1186/1741-7007-11-112. 792
- 707 35. Anna Sch nauer, Christian LB Paese, Maarten Hilbrant, Daniel J Leite, Evelyn E Schwa- 793
708 ger, Nat lia Martins Feitosa, Cornelius Eibner, Wim GM Damen, and Alistair P McGregor. 794
709 The wnt and delta-notch signalling pathways interact to direct pair-rule gene expression via 795
710 caudal during segment addition in the spider parasteatoda tepidariorum. *Development*, 143 796
711 (13):2455–2463, 2016. doi: 10.1242/dev.131656. 797
- 712 36. A Pikovsky, M Rosenblum, and J Kurths. Synchronization: a universal concept in nonlinear 798
713 science. 2002. 799
- 714 37. Yoshiki Kuramoto. *Chemical Oscillations, Waves, and Turbulence*, volume 19. Springer 800
715 Berlin Heidelberg, Berlin, Heidelberg, 1984. 801
38. Frederick R Cross and Eric D Siggia. Mode locking the cell cycle. 72(2):021910, 2005. 802
803 ISSN 1539-3755. doi: 10.1103/PhysRevE.72.021910.
39. Alexander Balanov, Natalia Janson, Dmitry Postnov, and Olga Sosnovitsea. *Synchroniza- 804*
805 *tion: from simple to complex*. Springer Science & Business Media, 2008.
40. Akira It . Perturbation theory of self-oscillating system with a periodic perturbation. 806
807 *Progress of Theoretical Physics*, 61(1):45–53, 1979. doi: 10.1143/PTP.61.45.
41. Tohru Kai and Kazuhisa Tomita. Stroboscopic phase portrait of a forced nonlinear oscillator. 808
809 *Progress of Theoretical Physics*, 61(1):54–73, 1979. doi: 10.1143/PTP.61.54.
42. F Buchholz, A Freund, and FW Schneider. Periodic perturbation of the bz-reaction in a cstr: 810
811 chemical resonance, entrainment and quasi-periodic behavior. In *Temporal Order*, pages 812
813 116–121. Springer, 1985. doi: 10.1007/978-3-642-70332-4_16.
43. Rabih Makki, Alberto P Mu uzuri, and Juan Perez-Mercader. Periodic perturbation of chem- 814
815 ical oscillators: Entrainment and induced synchronization. *Chemistry—A European Journal*, 816
817 20(44):14213–14217, 2014. doi: 10.1002/chem.201403647.
44. Adri n E Granada, Grigory Borydyugov, Achim Kramer, and Hanspeter Herzel. Human 818
819 chronotypes from a theoretical perspective. 8(3):e59464, 2013. doi: 10.1371/journal.pone.
820 0059464.
45. Adri n E Granada and Hanspeter Herzel. How to achieve fast entrainment? the timescale 821
822 to synchronization. 4(9):e7057, 2009. doi: 10.1371/journal.pone.0007057.
46. Marten Postma and Joachim Goedhart. PlotsOfData—A web app for visualizing data to- 823
824 gether with their summaries. *PLoS Biology*, 17(3):e3000202, 2019. ISSN 1544-9173. doi:
825 10.1371/journal.pbio.3000202.
47. Joachim Goedhart. Plotwiz: A web app for plotting and annotating continuous data. *PLoS 826*
827 *Biology*, 18(1):e3000581, 2020. doi: 10.1371/journal.pbio.3000581.
48. Namiko Mitarai, Uri Alon, and Mogens H Jensen. Entrainment of noise-induced and limit cycle 828
829 oscillators under weak noise. *Chaos: An Interdisciplinary Journal of Nonlinear Science*, 830
831 23(2):023125, 2013. doi: 10.1063/1.4808253.
49. EM Izhikevich. Dynamical systems in neuroscience. 2007.
50. Akihiro Isomura, Fumiko Ogushi, Hiroshi Kori, and Ryoichiro Kageyama. Optogenetic per- 832
833 turbation and bioluminescence imaging to analyze cell-to-cell transfer of oscillatory infor- 834
835 mation. 31(5):524–535, 2017. ISSN 0890-9369. doi: 10.1101/gad.294546.116.
51. A Granada, RM Hennig, B Ronacher, A Kramer, and H Herzel. *Chapter 1 Phase Response 836*
837 *Curves*, volume 454. 2009. ISBN 9780123745521. doi: 10.1016/s0076-6879(08)03801-9.
52. Collin S Pittendrigh and Victor G Bruce. An oscillator model for biological clocks. *Rhythmic 838*
839 *and synthetic processes in growth*, pages 75–109, 1957. doi: 10.1515/9781400876167-006.
53. Jrgen Aschoff and Hermann Pohl. Phase relations between a circadian rhythm and its 840
841 zeitgeber within the range of entrainment. *Naturwissenschaften*, 65(2):80–84, 1978. ISSN
842 0028-1042. doi: 10.1007/BF00440545.
54. Jan R mi, Martha Merrow, and Till Roenneberg. A circadian surface of entrainment: varying 843
844 t , τ , and photoperiod in neurospora crassa. *Journal of biological rhythms*, 25(5):318–328,
845 2010. doi: 10.1177/0748730410379081.
55. Grigory Borydyugov, Ute Abraham, Adrian Granada, Pia Rose, Katharina Imkeller, Achim 846
847 Kramer, and Hanspeter Herzel. Tuning the phase of circadian entrainment. 12(108):
848 20150282, 2015. ISSN 1742-5689. doi: 10.1098/rsif.2015.0282.
56. Arthur T Winfree. Biological rhythms and the behavior of populations of coupled oscillators. 849
850 16(1):15–42, 1967. ISSN 0022-5193. doi: 10.1016/0022-5193(67)90051-3.
57. A Kunysz, L Glass, and A Shrier. Overdrive suppression of spontaneously beating chick 851
852 heart cell aggregates: experiment and theory. *Am J Physiol*, 269(3 Pt 2):H1153–64, 1995.
58. L Jutras-Dub , E El-Sherif, and P Fran ois. Geometric models for robust encoding of dy- 853
854 namical information into embryonic patterns. *Elife*, 9, 2020.
59. Mary Jane West-Eberhard. *Developmental Plasticity and Evolution*. Oxford University 855
856 Press, 2003.
60. MW Meeuse, YP Hauser, LJ Morales Moya, GJ Hendriks, J Eglinger, G Bogaarts, C Tsi- 857
858 airis, and H Grof hans. Developmental function and state transitions of a gene expression
859 oscillator in caenorhabditis elegans. *Mol Syst Biol*, 16(7):e9498, 2020.
61. Julian Lewis. Autoinhibition with transcriptional delay a simple mechanism for the zeb- 860
861 rafish somitogenesis oscillator. 13(16):1398–1408, 2003. ISSN 0960-9822. doi: 10.1016/
862 S0960-9822(03)00534-7.
62. Sa l Ares, Luis G Morelli, David J J rg, Andrew C Oates, and Frank J licher. Collective 863
864 modes of coupled phase oscillators with delayed coupling. *Phys Rev Lett*, 108(20):204101,
865 2012. ISSN 1079-7114. doi: 10.1103/PhysRevLett.108.204101.
63. Takeharu Nagai, Keiji Ibatata, Eun Sun Park, Mie Kubota, Katsuhiko Mikoshiba, and Atsushi 866
867 Miyawaki. A variant of yellow fluorescent protein with fast and efficient maturation for cell-
868 biological applications. *Nature biotechnology*, 20(1):87–90, 2002. doi: 10.1038/nbt0102-87.
64. Aixa V Morales, Yuko Yasuda, and Ish-Horowitz, David. Periodic lunatic fringe expression 869
870 is controlled during segmentation by a cyclic transcriptional enhancer responsive to notch
871 signaling. 3(1):63–74, 2002. ISSN 1534-5807. doi: 10.1016/S1534-5807(02)00211-3.
65. Susan E Cole, John M Levorse, Shirley M Tilghman, and Thomas F Vogt. Clock regulatory 872
873 elements control cyclic expression of lunatic fringe during somitogenesis. 3(1):75–84, 2002.
874 ISSN 1534-5807. doi: 10.1016/S1534-5807(02)00212-5.
66. Scott Rogers, Rodney Wells, and Martin Rechsteiner. Amino acid sequences common to 875
876 rapidly degraded proteins: the pest hypothesis. *Science*, 234(4774):364–368, 1986. doi:
877 10.1126/science.2876518.
67. Marek J van Oostrom, Wilke HM Meijer, and Katharina F Sonnen. A microfluidics approach 878
879 for the functional investigation of signaling oscillations governing somitogenesis. *JOVE-*
880 *JOURNAL OF VISUALIZED EXPERIMENTS*, (169), 2021. doi: 10.3791/62318.
68. Bachir El Debs, Ramesh Utharala, Irina V Balyasnikova, Andrew D Griffiths, and Christoph A 881
882 Merten. Functional single-cell hybridoma screening using droplet-based microfluidics.
883 *Proceedings of the National Academy of Sciences*, 109(29):11570–11575, 2012. doi:
884 10.1073/pnas.1204514109.
69. Antonio Z Politi, Yin Cai, Nike Walther, M Julius Hossain, Birgit Koch, Malte Wachsmuth, 885
886 and Jan Ellenberg. Quantitative mapping of fluorescently tagged cellular proteins using
887 fcs-calibrated four-dimensional imaging. *Nature protocols*, 13(6):1445–1464, 2018. doi:
888 10.1038/nprot.2018.040.
70. Johannes Schindelin, Ignacio Arganda-Carreras, Erwin Frise, Verena Kaynig, Mark Longair, 889
890 Tobias Pietzsch, Stephan Preibisch, Curtis Rueden, Stephan Saalfeld, Benjamin Schmid,

- 802 et al. Fiji: an open-source platform for biological-image analysis. *Nature methods*, 9(7):
803 676–682, 2012. doi: 10.1038/nmeth.2019.
- 804 71. Gregor Mönke, Frieda A Sorgenfrei, Christoph Schmal, and Adrián E Granada. Optimal
805 time frequency analysis for biological data-pyboat. *bioRxiv*, 2020. doi: 10.1101/2020.04.29.
806 067744.
- 807 72. John D Hunter. Matplotlib: A 2d graphics environment. *Computing in science & engineering*,
808 9(3):90–95, 2007. doi: 10.1109/MCSE.2007.55.
- 809 73. Stéfan van der Walt, S Chris Colbert, and Gael Varoquaux. The numpy array: a structure for
810 efficient numerical computation. *Computing in science & engineering*, 13(2):22–30, 2011.
811 doi: 10.1109/MCSE.2011.37.
- 812 74. Charles R. Harris, K. Jarrod Millman, Stéfan J. van der Walt, Ralf Gommers, Pauli Virta-
813 nen, David Cournapeau, Eric Wieser, Julian Taylor, Sebastian Berg, Nathaniel J. Smith,
814 Robert Kern, Matti Picus, Stephan Hoyer, Marten H. van Kerkwijk, Matthew Brett, Allan
815 Haldane, Jaime Fernández del Río, Mark Wiebe, Pearu Peterson, Pierre Gérard-Marchant,
816 Kevin Sheppard, Tyler Reddy, Warren Weckesser, Hameer Abbasi, Christoph Gohlke, and
817 Travis E. Oliphant. Array programming with NumPy. *Nature*, 585(7825):357–362, Septem-
818 ber 2020. ISSN 1476-4687. doi: 10.1038/s41586-020-2649-2.
- 819 75. Wes McKinney et al. Data structures for statistical computing in python. In *Proceedings of*
820 *the 9th Python in Science Conference*, volume 445, pages 51–56. Austin, TX, 2010. doi:
821 10.25080/Majora-92bf1922-00a.
- 822 76. Stéfan van der Walt, Johannes L Schönberger, Juan Nunez-Iglesias, François Boulogne,
823 Joshua D Warner, Neil Yager, Emmanuelle Gouillart, and Tony Yu. scikit-image: image
824 processing in python. *PeerJ*, 2:e453, 2014. doi: 10.7717/peerj.453.
- 825 77. Pauli Virtanen, Ralf Gommers, Travis E Oliphant, Matt Haberland, Tyler Reddy, David Cour-
826 napeau, Evgeni Burovski, Pearu Peterson, Warren Weckesser, Jonathan Bright, et al. Scipy
827 1.0: fundamental algorithms for scientific computing in python. *Nature methods*, 17(3):261–
828 272, 2020. doi: 10.1038/s41592-019-0686-2.
- 829 78. Michael Waskom, Olga Botvinnik, Paul Hobson, John B. Cole, Yaroslav Halchenko, Stephan
830 Hoyer, Alistair Miles, Tom Augspurger, Tal Yarkoni, Tobias Megies, Luis Pedro Coelho,
831 Daniel Wehner, cynddl, Erik Ziegler, diego0020, Yury V. Zaytsev, Travis Hoppe, Skipper
832 Seabold, Phillip Cloud, Miikka Koskinen, Kyle Meyer, Adel Qalieh, and Dan Allan. seaborn:
833 v0.5.0 (november 2014), November 2014.
- 834 79. Marten Postma and Joachim Goedhart. PlotsOfData—A web app for visualizing data to-
835 gether with their summaries. *Plos Biol*, 17(3):e3000202, 2019. ISSN 1544-9173. doi:
836 10.1371/journal.pbio.3000202.
- 837 80. Moreno-Risueno, Miguel, Jaimie Norman, Antonio Moreno, Jingyuan Zhang, Sebastian Ah-
838 nert, and Philip Benfey. Oscillating gene expression determines competence for periodic
839 arabidopsis root branching. *Science*, 329(5997):1306–1311, 2010. ISSN 0036-8075. doi:
840 10.1126/science.1191937.

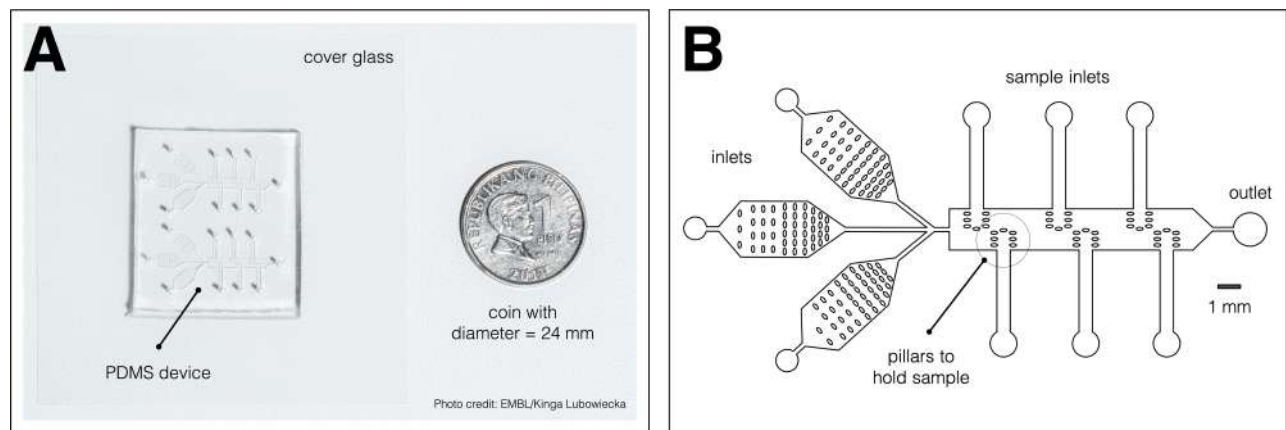


Fig. S1. A microfluidics device for simultaneous culture, imaging, and entrainment of the segmentation clock in 2D-assays. (A) Photo of the chip, previously described in (1), bonded to cover glass and a coin (diameter: 24 mm) for scale. The split layout separating the upper and lower channel systems allows simultaneous delivery of drug and DMSO control to samples on opposite sides of the same device. Photo credit: EMBL/Kinga Lubowiecka. (B) Design of the microfluidics chip, showing inlets for medium and drug, inlets for the samples, pillars to hold each sample, and an outlet.

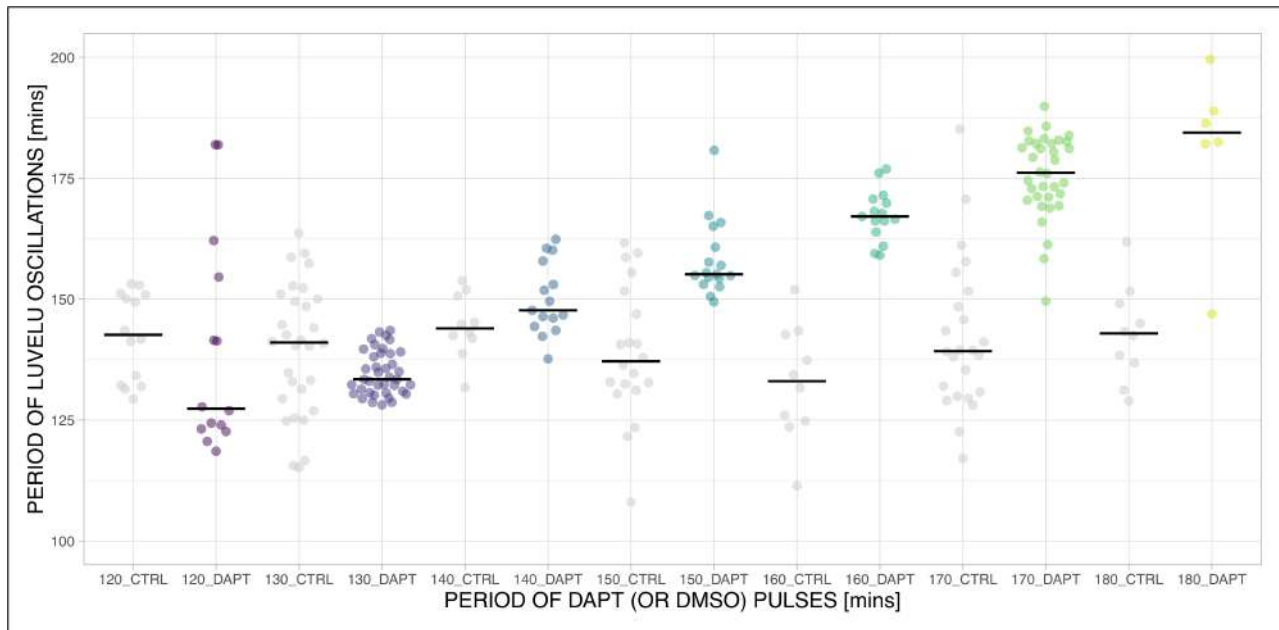


Fig. S2. The period of the segmentation clock can both be sped up and slowed down by modulating the period of DAPT pulses. Mean period from 650 to 850 mins after start of the experiment of samples subjected to periodic pulses of 2 μ M DAPT (or DMSO for controls). Each sample is represented as a dot, while the median of all samples is denoted as a solid horizontal line. The period of the DAPT (or DMSO) pulses is specified. **120-min:** (CTRL: $n = 30$ and $N = 8$) and (DAPT: $n = 14$ and $N = 3$), **130-min:** (CTRL: $n = 30$ and $N = 8$) and (DAPT: $n = 39$ and $N = 10$), **140-min:** (CTRL: $n = 10$ and $N = 3$) and (DAPT: $n = 15$ and $N = 3$), **150-min:** (CTRL: $n = 20$ and $N = 4$) and (DAPT: $n = 17$ and $N = 4$), **160-min:** (CTRL: $n = 10$ and $N = 3$) and (DAPT: $n = 15$ and $N = 3$), **170-min:** (CTRL: $n = 24$ and $N = 7$) and (DAPT: $n = 34$ and $N = 8$), **180-min:** (CTRL: $n = 10$ and $N = 2$) and (DAPT: $n = 6$ and $N = 1$). Data were visualized using PlotsOfData (46).

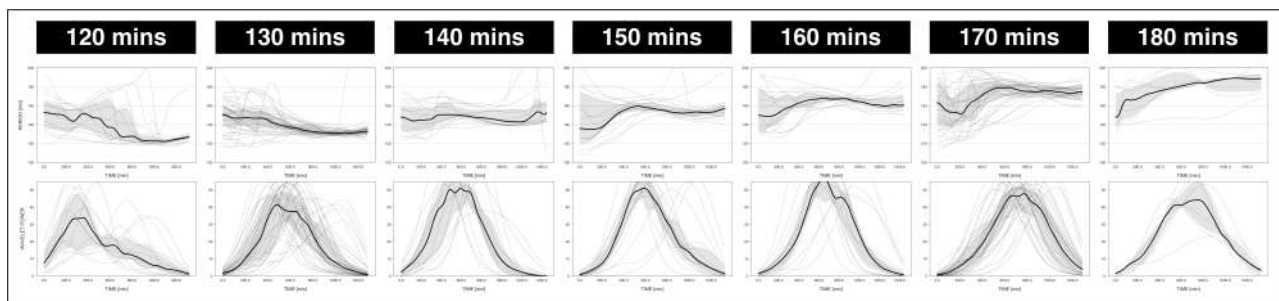


Fig. S3. The period of the segmentation clock becomes locked to the period of the DAPT pulses. The period and wavelet power of the oscillations, obtained via wavelet analysis, are plotted across time. Each sample and their median are represented here as a dashed line and a solid line, respectively. The gray shaded area corresponds to the interquartile range. The period of the 2 μ M DAPT pulses is specified. **120-min:** $n = 14$ and $N = 3$, **130-min:** $n = 39$ and $N = 10$, **140-min:** $n = 15$ and $N = 3$, **150-min:** $n = 17$ and $N = 4$, **160-min:** $n = 15$ and $N = 3$, **170-min:** $n = 34$ and $N = 8$, **180-min:** $n = 6$ and $N = 1$. The period evolution plots for the 130-min and 170-min conditions are the same as the period evolution plots for the 2 μ M condition in Figure S4A and Figure 4B, respectively.

Table S1. Summary statistics on period-locking of the segmentation clock in E10.5 2D-assays to periodic pulses of 2 μ M DAPT. This table summarizes the median, 95% confidence interval (CI) of the median, mean, standard deviation (SD), and standard error of the mean (SEM) of the segmentation clock in 2D-assays subjected to periodic pulses of 2 μ M DAPT. These summary statistics were determined using PlotsOfData (46). A plot of these data is shown in Figure 3D.

Pulse Period	n	N	Median, mins	95% CI of Median, mins	Mean, mins	SD, mins	SEM, mins
120 mins	14	3	127.36	123.16 – 148.03	139.39	22.28	6.18
130 mins	39	10	133.44	132.21 – 135.97	134.75	4.56	0.74
140 mins	15	3	147.68	146.10 – 153.02	150.00	7.42	1.98
150 mins	17	4	155.14	154.33 – 160.74	158.18	7.77	1.94
160 mins	15	3	167.09	166.16 – 169.84	167.33	5.28	1.41
170 mins	34	8	176.14	173.06 – 181.20	175.56	8.52	1.48
180 mins	6	1	184.43	164.54 – 194.21	181.06	17.88	8.00

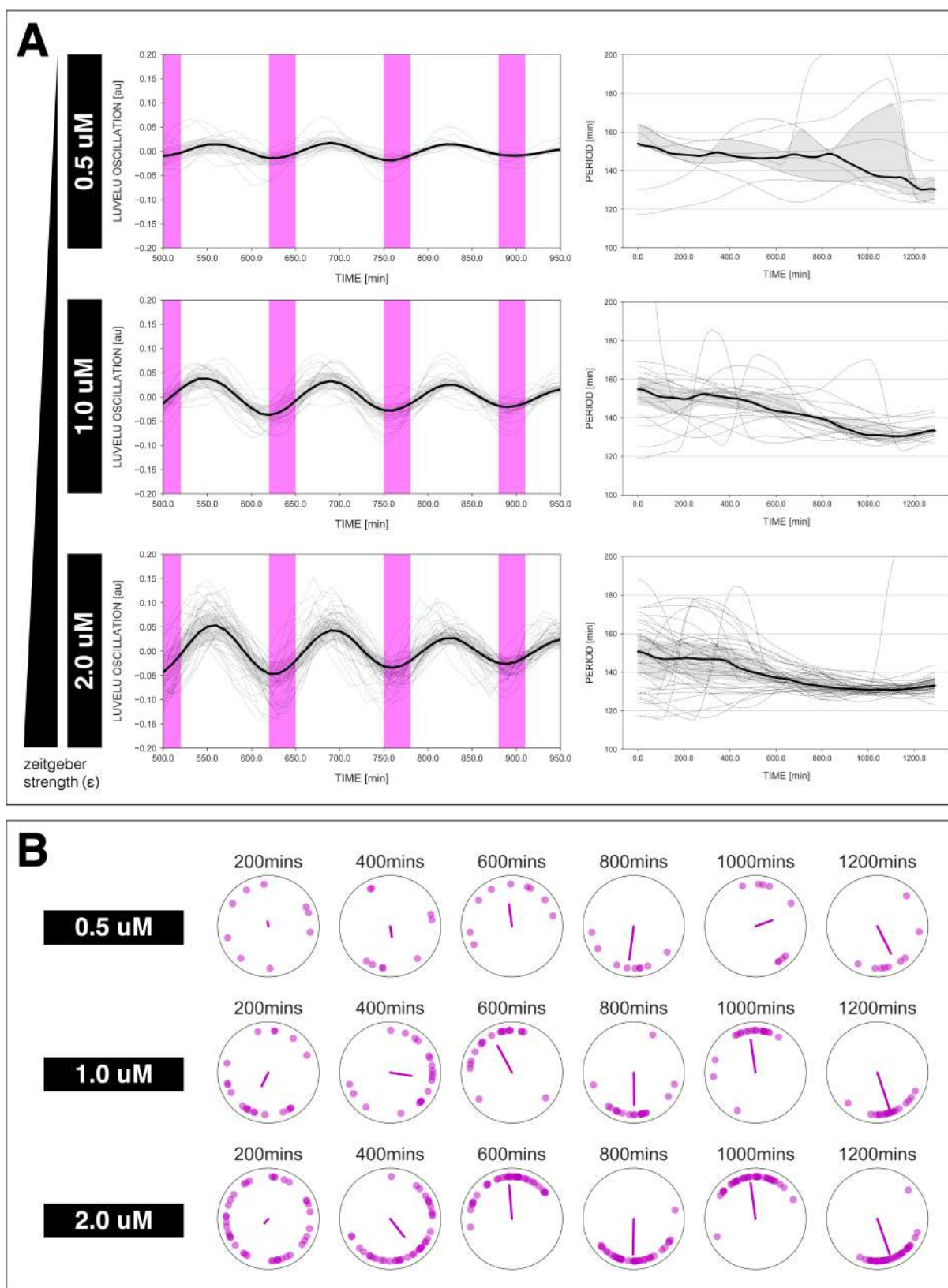


Fig. S4. Changing the concentration of DAPT, equivalent to changing zeitgeber strength, affects entrainment of the segmentation clock to 130-min periodic DAPT pulses. (A) Left: Detrended timeseries of the segmentation clock in 2D-assays entrained to 130-min periodic pulses of either 0.5 μM , 1 μM , or 2 μM DAPT, zoomed in from 500 mins to 950 mins. Periodic pulses are indicated as magenta bars and the timeseries of each sample (for 0.5 μM : $n = 9$ and $N = 2$, for 1 μM : $n = 20$ and $N = 4$, for 2 μM : $n = 39$ and $N = 10$) is marked with a dashed line. The median of the oscillations is represented here as a solid line, while the gray shaded area denotes the interquartile range. Right: Period evolution during entrainment, obtained from wavelet analysis. The period evolution for each sample and the median of the periods are represented here as a dashed line and a solid line, respectively. The gray shaded area corresponds to the interquartile range. (B) Polar plots at different timepoints showing phase of each sample and their first Kuramoto order parameter, represented as a magenta dot along the circumference of a circle and a magenta line segment at the circle's center, respectively. A longer line segment corresponds to a higher first Kuramoto order parameter, and thus to more coherent samples. The direction of the line denotes the vectorial average of the sample phases. Time is indicated as mins elapsed from the start of the experiment.

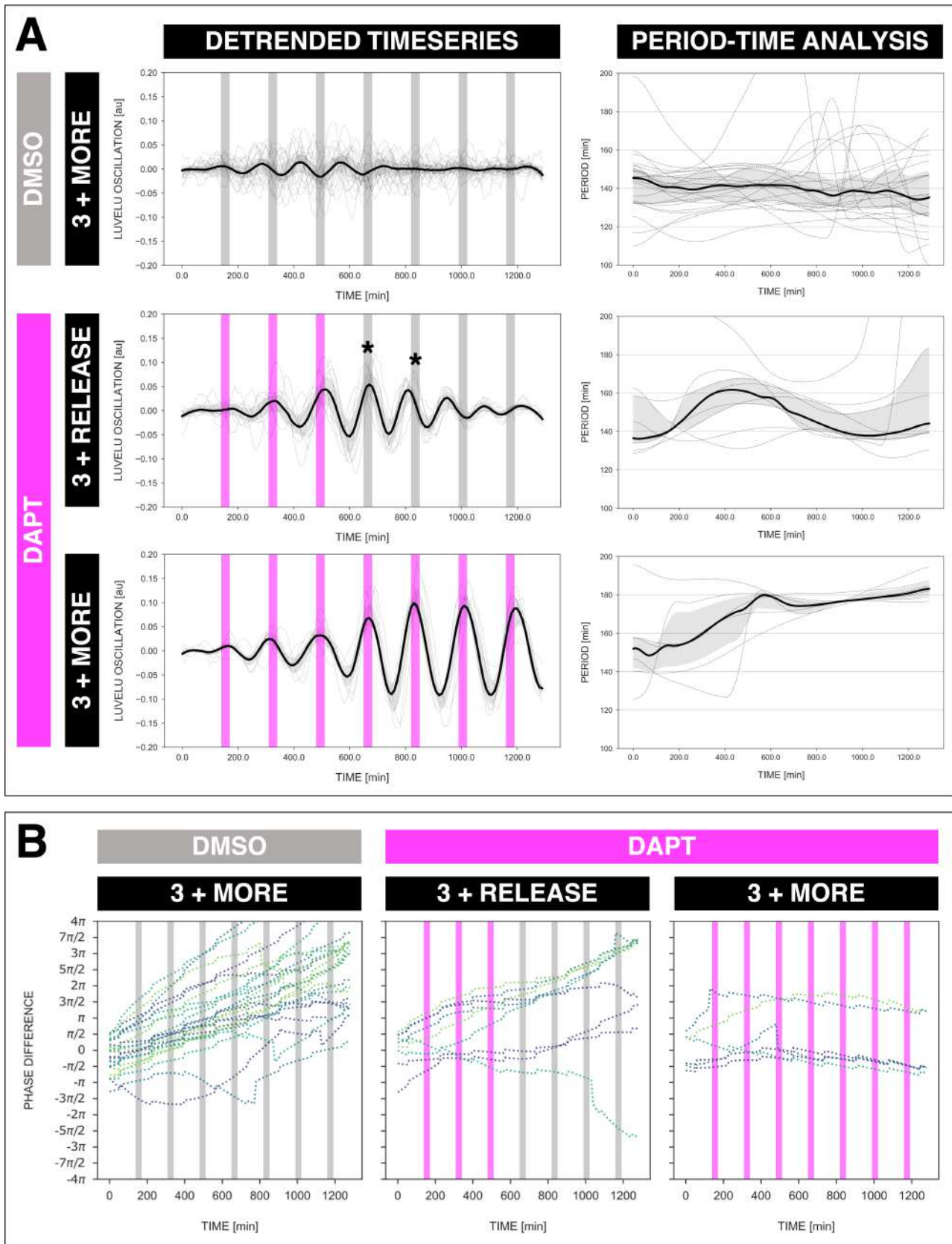


Fig. S5. The segmentation clock keeps its adjusted rhythm even a few cycles after release from DAPT pulses. (A) Left: Detrended timeseries of the segmentation clock in 2D-assays subjected to 170-min periodic pulses of DMSO (gray bars) and/or 2 μ M DAPT (magenta bars). The timeseries of each sample (for continuous DMSO pulses: $n = 24$ and $N = 7$, for 3 DAPT pulses and then release: $n = 9$ and $N = 2$, for continuous DAPT pulses: $n = 6$ and $N = 2$) is marked with a dashed line. The median of the oscillations is represented here as a solid line, while the gray shaded area denotes the interquartile range. Right: Period evolution during entrainment, obtained from wavelet analysis. The period evolution for each sample and the median of the periods are represented here as a dashed line and a solid line, respectively. The gray shaded area corresponds to the interquartile range. Data for the continuous DMSO pulses are the same as the controls in Figure 3A-B. (B) Phase difference between the segmentation clock and the drug pulses. Note that a phase of $-\pi/2$ is equivalent to a phase of $3\pi/2$, and a phase of 0 is equivalent to a phase of 2π . Periodic pulses of DMSO and 2 μ M DAPT are indicated as gray bars and as magenta bars, respectively. Each sample within each condition is marked with different colors.

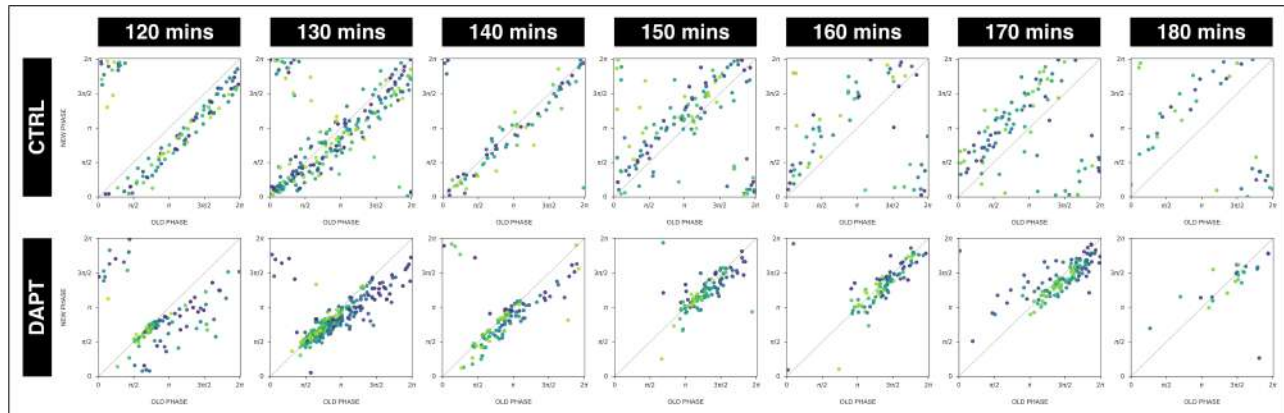


Fig. S6. The segmentation clock establishes a stable phase relationship with the periodic DAPT pulses. Stroboscopic maps summarizing phase dynamics when the segmentation clock was subjected to periodic pulses of 2 μM DAPT (or DMSO for controls). The period of the DAPT (or DMSO) pulses is specified. Colors mark progression in time, from purple to yellow. **120-min:** (CTRL: $n = 14$ and $N = 3$) and (DAPT: $n = 14$ and $N = 3$), **130-min:** (CTRL: $n = 30$ and $N = 8$) and (DAPT: $n = 39$ and $N = 10$), **140-min:** (CTRL: $n = 10$ and $N = 3$) and (DAPT: $n = 15$ and $N = 3$), **150-min:** (CTRL: $n = 20$ and $N = 4$) and (DAPT: $n = 17$ and $N = 4$), **160-min:** (CTRL: $n = 10$ and $N = 3$) and (DAPT: $n = 15$ and $N = 3$), **170-min:** (CTRL: $n = 24$ and $N = 7$) and (DAPT: $n = 34$ and $N = 8$), **180-min:** (CTRL: $n = 10$ and $N = 2$) and (DAPT: $n = 6$ and $N = 1$).

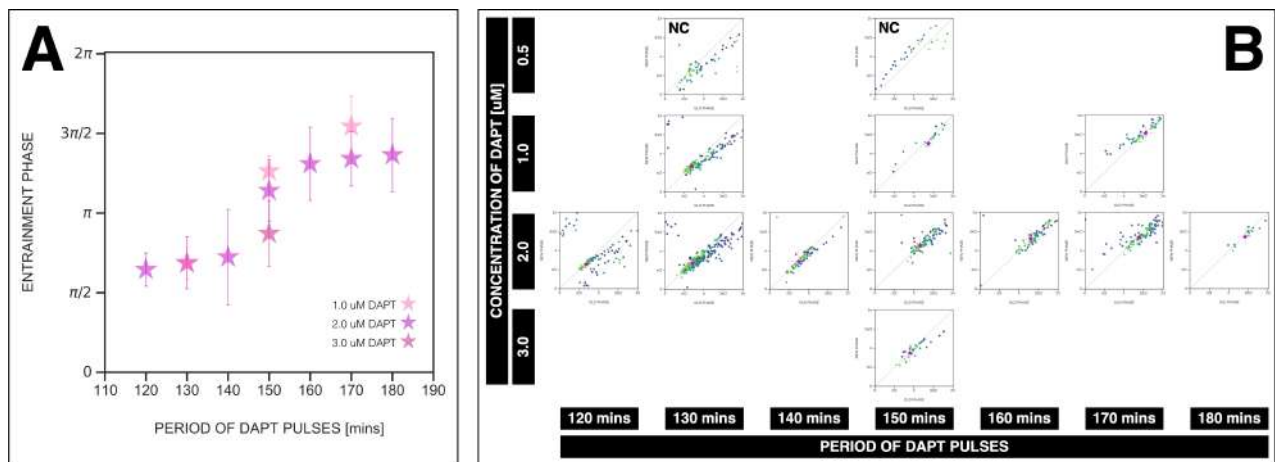


Fig. S7. *Zeitgeber* period and *zeitgeber* strength affect the entrainment phase of the segmentation clock. (A) Entrainment phase at different periods of DAPT pulses (i.e. *zeitgeber* period) and different drug concentrations (i.e. *zeitgeber* strength). Entrainment phase (ϕ_{ent}) was calculated from the vectorial average of the phases of phase-locked samples at the time corresponding to last considered DAPT pulse. A sample was considered phase-locked if the difference between its phase at the time of the final drug pulse considered and its phase one drug pulse before is less than $\pi/8$ – for 120-min: (2 μM : $n = 13/14$ and $N = 3/3$), for 130-min: (1 μM : $n = 17/20$ and $N = 4/4$), (2 μM : $n = 38/39$ and $N = 10/10$), for 140-min: (2 μM : $n = 10/15$ and $N = 3/3$), for 150-min: (1 μM : $n = 3/4$ and $N = 1/1$), (2 μM : $n = 16/17$ and $N = 4/4$), (3 μM : $n = 5/5$ and $N = 1/1$), for 160-min: (2 μM : $n = 11/15$ and $N = 3/3$), for 170-min: (1 μM : $n = 12/18$ and $N = 4/5$), (2 μM : $n = 28/34$ and $N = 8/8$), for 180-min: (2 μM : $n = 4/6$ and $N = 1/1$). The spread of ϕ_{ent} between samples is reported in terms of the circular standard deviation ($\sqrt{-2\ln R}$, where R is the first Kuramoto order parameter). Colors mark concentration of DAPT. Drug pulse duration was kept constant at 30 mins/cycle. (B) Stroboscopic maps for different values of *zeitgeber* period and *zeitgeber* strength placed next to each other. The localized region close to the diagonal in each map marks ϕ_{ent} for that condition. This is highlighted with a magenta star, which corresponds to the centroid of the said region. The centroid (x_c, y_c) was calculated from the vectorial average of the phases of phase-locked samples at the end of the experiment, where x_c = vectorial average of old phase, y_c = vectorial average of new phase. The spread of the points in the region is reported in terms of the circular standard deviation ($\sqrt{-2\ln R}$, where R is the first Kuramoto order parameter). The period of the DAPT pulses and the concentration of DAPT are indicated. Colors mark progression in time, from purple to yellow. NC means not considered (in plotting panel A) because no/small fraction of samples was phase-locked – for 0.5 μM 130-min: $n = 4/9$ and $N = 2/2$, for 0.5 μM 150-min: $n = 0/6$ and $N = 0/1$. Stroboscopic maps for these NC conditions include all samples, unlike the other conditions where only phase-locked samples are plotted. Data for 2 μM condition is the same as that in Figure 7A-B.

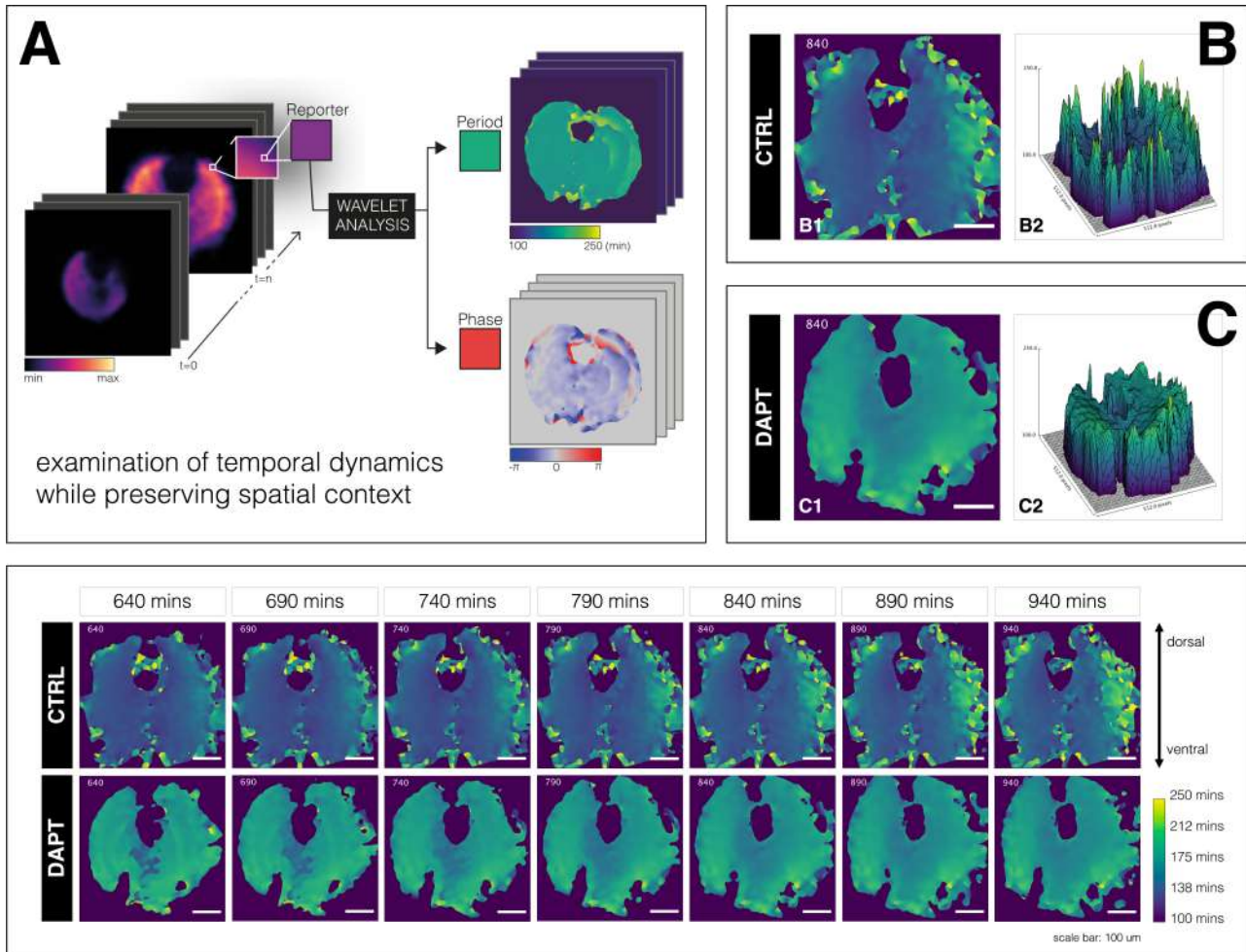


Fig. S8. A spatial period gradient, though altered, emerges in the tissue even upon entrainment of the segmentation clock to a slower period. Left: Schematic of pipeline to generate period and phase movies using pixel-by-pixel wavelet analysis (A). Illustration by Stefano Vianello. **Right:** Snapshot of period wavelet movie of control subjected to 170-min periodic pulses of DMSO (B) or entrained sample subjected to 170-min periodic pulses of 2 μ M DAPT (C), taken at 840 mins after the start of experiment. Period is either shown using heatmap (B1,C1) or as a surface plot (B2,C2). **Bottom:** Snapshots of period wavelet movie of samples in (B) and (C) at different time points. Time is indicated as mins elapsed from the start of the experiment. Sample is rotated so that the dorsal side is up.

Supplementary Note 1: Materials and methods

A. Mouse lines. For most of the experiments in this study, we used a transgenic mouse line expressing a dynamic Notch signaling reporter driven from the *Lfng* promoter, more commonly known as LuVeLu. The generation of LuVeLu was previously described (14). Briefly, the expression of Venus, an improved version of YFP (63), was driven from a 2-kb fragment of the *Lfng* promoter (64, 65). The locus was flanked by *Lfng* 3'-UTR and a modified PEST domain (66) to destabilize the reporter mRNA and protein, respectively.

Axin2-linker-Achilles, a mouse line expressing Axin2 fused with a GSAGS linker to Achilles, a fast-maturing variant of YFP (22), was generated in-house. To generate the knock-in alleles, we targeted the stop codon of endogenous Axin2 locus with vector containing the reporter sequence coding for Achilles and a selection cassette. This targeting vector was constructed as follows: linker-Achilles-loxP-PGK Neo-loxP. The selection cassette was flanked by loxP- sites for eventual Cre-mediated excision. Axin2-linker-Achilles knock-in reporter line was generated by standard gene targeting techniques using R1 embryonic stem cells. Briefly, chimeric mice were obtained by C57BL/6 blastocyst injection and then outbred to establish the line through germline transmission. The Achilles/pRSETB plasmid was a gift from the lab of Atsushi Miyawaki at RIKEN Center for Brain Science (RIKEN-CBS) in Japan.

Mice were kept in an outbred background and were housed in the EMBL Laboratory Animal Resources (LAR). All animal experiments were conducted under veterinarian supervision and after project approval by European Molecular Biology Laboratory, following the guidelines of the European Commission, Directive 2010/63/EU and AVMA Guidelines 2007.

B. Media preparation. On the day of the experiment, dissection medium and culture medium were freshly prepared as indicated in Table S2. Culture medium was filter sterilized using a PVDF filter (pore size: 0.22 μ m, Merck). Both dissection medium and culture medium were equilibrated to 37°C for at least 15 minutes, and were kept in a 37°C incubator under 5% CO₂ until use.

Table S2. Recipe for media preparation. Formulations specified here are for the preparation of approximately 50 mL of medium. Special DMEM/F12* used in these media does not contain glucose, L-glutamine, sodium pyruvate, and phenol red. Culture medium is filter sterilized after preparation.

Component	Dissection Medium	Culture Medium
BSA (Equitech-Bio, BAC62)	0.5 g	0.02 g
DMEM/F12* (Cell Culture Technologies)	50 mL	50 mL
1 M HEPES (Gibco, 15630-106)	1 mL	–
10000 U/mL PenStrep (Gibco, 15140-122)	–	500 μ L
45% Glucose (Sigma, G8769)	44.4 μ L	44.4 μ L
200 mM L-Glutamine (Gibco, 25030-081)	500 μ L	500 μ L

C. Mouse dissection and embryo recovery. Female mice were sacrificed on 10.5 dpc (days post coitum) via cervical dislocation. The skin on their ventral side (belly area) was wiped with 70% ethanol, and an incision was made using a clean pair of surgical scissors. The uterine horns were harvested and were washed once with dissection medium. In dissection medium, under a stereo microscope (Leica M80), the deciduae were cut open using clean forceps and the embryos were recovered. The embryos were again washed with fresh dissection medium and their tails were clipped using forceps. Clipped tails were then transferred to a new dish with fresh dissection medium. The volume of dissection medium in the dish was kept to minimum to lessen autofluorescence, which could interfere with subsequent screening. The tails were then screened for presence of the reporter-of-interest (e.g. LuVeLu) using a stereo fluorescence microscope.

The tailbud was cut from the rest of the tail and was immediately transferred to pre-equilibrated culture medium that was supplemented with HEPES (170 μ L of 1 M HEPES in 10 mL culture medium). These isolated embryonic tissues were then directly loaded in the microfluidics device.

D. Preparations for microfluidics-based entrainment of 2D-assays. We used in this study a microfluidics-based experimental entrainment platform with a general protocol elaborated in a recent publication (67). The PDMS microfluidics device was made using standard soft lithography (68) and as previously described (1). The ratio of Sylgard 184 silicone elastomer base (Dow) to curing agent (Dow) was 9:1 (w/w). PDMS chip was attached to cover glass (70 mm x 70 mm, 1.5H, Marienfeld 0107999 098) via plasma bonding.

881 **UV irradiation of PTFE tubing and PDMS device**

882 PTFE tubing (inner diameter: 0.6 mm, APT AWG24T) and syringe needles (22G 1 1/4 - Nr. 12), as summarized in Table
 883 S3, were prepared a day prior to actual microfluidics-based entrainment experiment. In addition to 1 PDMS microfluidics
 884 device (Figure S1B), each experiment required 4 3-meter PTFE tubing (each with syringe needle inserted in one end) for the
 885 drug/medium inlets, 2 1-meter PTFE tubing (each with syringe needle inserted in one end) for the outlets, and 24 1-centimeter
 886 plugs made from cut PDMS-filled PTFE tubing for the sample inlets and unused drug/medium inlets. These were all sterilized
 887 under UV for at least 20 minutes.
 888

Table S3. List of PTFE tubing needed for a microfluidics-based entrainment experiment. For the first two items, a syringe needle is to be inserted inside one end of each tubing. Plugs are made from cut PDMS-filled PTFE tubing, and are used to seal inlets after sample loading. Controls are already taken into account in the specified quantities.

Item	With Needle?	Quantity	Use
3-meter PTFE tubing	Y	4	drug/medium inlet
1-meter PTFE tubing	Y	2	outlet
1-centimeter plug	N	24	sample inlet + unused drug/medium inlet

889
 890 **Fibronectin-coating of PDMS device and overnight soaking in buffer**

891 While waiting, 5 mL of PenStrep (Gibco, 15140-122) was added to 495 mL of 1x PBS (PBS+PenStrep). 5.6 mL of the
 892 buffer was set aside to prepare fibronectin solution, while the rest was poured in a glass dish. After UV irradiation, the
 893 sterilized PDMS device was immersed in the PBS+PenStrep and bubbles were removed by flushing the channels with buffer.
 894 PDMS-filled PTFE plugs were also immersed in PBS+PenStrep. To prepare the fibronectin solution, 280 uL of fibronectin
 895 (Sigma-Aldrich, F1141) was added to the set aside 5.6 mL PBS+PenStrep. At least 2.5 mL of fibronectin solution was loaded
 896 into a 3 mL syringe (diameter: 8.66 mm, BD Luer-Lok REF 309658). A UV-irradiated needle, which was earlier inserted
 897 into a 1-meter PTFE tubing, was attached to the filled syringe. The tubing was then inserted into an outlet in the PDMS
 898 device, carefully avoiding introduction of bubbles. Fibronectin was flowed (flow rate: 50 uL/hr) into the PDMS device at room
 899 temperature overnight.
 900

901 **Preparation of syringes containing drug/medium**

902 For a microfluidics-based experiment with periodic pulses of drug, four 10 mL syringes (diameter: 14.5 mm, BD Luer-Lok
 903 REF 300912) were filled with either the drug, DMSO control, or culture medium (see Table S2). Components of solution in
 904 each of these syringes are specified in Table S4. Drug used in this study was DAPT (Sigma-Aldrich, D5942-5MG). To prepare
 905 10 mM stock of DAPT, 5 mg DAPT (MW = 432.46 g/mol) was dissolved in 1156.2 uL DMSO (Sigma-Aldrich, D8418). This
 906 was aliquoted and stored at -20°C until use.

Table S4. List of syringe containing drug/medium for a microfluidics-based entrainment experiment. Formulations specified here are for any drug with final concentration X uM. For recipe to prepare culture medium, please refer to Table S2.

Component	Syringe A DRUG	Syringe B CONTROL	Syringe C MEDIUM	Syringe D MEDIUM
Drug (10 mM in DMSO)	X uL	-	-	-
DMSO (Sigma-Aldrich, D8418)	-	X uL	-	-
Cascade Blue (Invitrogen, C-3239)	2 uL	2 uL	-	-
Culture medium (see Table S2)	dilute to 10 mL	dilute to 10 mL	10 mL	10 mL

907
 908 **Degassing drug/medium and PDMS device**

909 After coating and overnight soaking, the PTFE tubing was cut away from the needle and was immediately immersed in the
 910 buffer. The dish containing immersed PDMS device, with attached tubing for the two outlets, and plugs were placed inside a
 911 vacuum desiccator chamber. The plunger of each syringe containing the drug/medium was pulled to maximum. The syringes
 912 were then also placed in the vacuum chamber, almost vertically, with the plunger resting on the desiccator. These were degassed
 913 under high pressure for at least 1.5 hours.

914 **E. Loading embryonic tissues in microfluidics device and mounting for live imaging.** Before mouse dissection and
915 recovery of mouse embryos, syringes containing the degassed drug/medium were each connected to a UV-irradiated 3-meter
916 PTFE tubing via attached syringe needle, and were carefully mounted on programmable pumps (World Precision Instruments,
917 AL-400) next to the microscope. Gas in the tubing was displaced with drug/medium by careful pushing of the syringes' plunger.
918 Pumps were turned on and flow rate was set to 900 $\mu\text{L/hr}$. The microscope was then equilibrated to 37°C and 5% CO_2 .
919 After recovery of embryonic tissues, using a pipette (i.e. P200 for 2D-assays and P1000 for intact PSM), each sample was
920 carefully loaded into the microfluidics device, which was already coated with fibronectin, immersed in a buffer of PBS and
921 PenStrep, and degassed. Each sample inlet was plugged with a PDMS-filled PTFE tubing immediately after sample loading.
922 Unused inlets, if any, were also plugged.
923 Flow rate of drug/medium was set to 20 $\mu\text{L/hr}$ and the tubings were carefully inserted into the drug/medium inlets in the PDMS
924 device while it is immersed in buffer. The tubings connected to the syringes with medium were inserted first, and the tubing
925 connected to the syringe with the drug was inserted last. A 15-min timer was started after insertion of the drug tubing. PDMS
926 device was then removed from the buffer and excess liquid on the cover glass was removed carefully with lint-free wipes
927 (Kimberly-Clark). The PDMS device, with more than 1 m of attached tubings, was carefully placed inside a pre-equilibrated
928 microfluidics holder (EMBL Mechanical Workshop, Figure S9) customized to fit the 70 mm x 70 mm cover glass (Marienfeld
929 0107999 098) and some PTFE tubing. Putting some of the tubing inside the microfluidics holder was necessary to equilibrate
930 the drug/medium to desired environmental conditions before they are perfused into the microfluidics device. The cover glass
931 was secured in place with grease and a U-shaped metal clamp. The microfluidics holder was then carefully mounted on the
932 stage of the microscope, and the end of the outlet tubings were placed in a beaker.
933 Fifteen minutes after insertion of the drug tubing in the PDMS device, each pump was tilted on its side and was equilibrated
934 for another 15 mins. Afterwards, the pump mounting the syringes with the drug and DMSO control was turned off, and the
935 pump mounting the syringes with the medium was set to flow rate of 60 $\mu\text{L/hr}$. Samples were equilibrated at these conditions
936 for at least 30 mins before start of imaging/entrainment.

937 **F. Setting up automated pumping.** Entrainment via periodic pulses of drug was performed through alternate perfusion of
938 medium and drug into the microfluidics device. Perfusion of drug/medium was done using syringes mounted on programmable
939 syringe pumps (World Precision Instruments, AL-400). Diameter of syringe (14.5 mm for 10-mL syringe, BD Luer-Lok REF
940 300912) was accordingly set to match a defined flow rate and a specified volume of solution to be perfused with the duration
941 of perfusion. Standard pumping programs of medium and drug/control are summarized in Tables S5 and S6, respectively,
942 considering an entrainment experiment with $T_{zeit} = 170$ mins.
943
944

945 **G. Confocal microscopy.** For most of the experiments here, samples were imaged in an LSM 780 laser-scanning mi-
946 croscope (Carl Zeiss Microscopy) fitted with an incubation chamber (EMBL Mechanical Workshop). A Plan-Apochromat
947 20x air objective with a numerical aperture (NA) of 0.8 (Carl Zeiss Microscopy) was used for imaging, and the zoom
948 was set to 0.6. Three z-stacks (spacing: 8 μm) were scanned for each sample every 10 mins to acquire timelapse movies.
949 Imaging of multiple samples in multiple locations was done with a motorized stage, controlled using Zen Black software
950 (Carl Zeiss Microscopy), and automated using a VBA macro developed by Antonio Politi (69), which is available at
951 <https://git.embl.de/grp-ellenberg/mypic>. The dimension of the images was 512 pixels x 512 pixels, with a
952 pixel size of 1.38 μm and bit depth of 16-bit. Detection of drug pulses, using Cascade Blue (excited with 405 nm) added to
953 the solution, was also done every 10 mins with lower image resolution: 1 z-stack, 32 pixel x 32 pixel (pixel size = 22.14 μm).
954 Imaging and automated pumping of drug/medium through the microfluidics device were started simultaneously.
955
956

957 **H. Data analysis.** Details on the coarse-graining strategy and analyses of entrainment dynamics are specified here.

958 **Extracting timeseries from global intensity of 2D-assays for subsequent analyses**

959 To extract the timeseries corresponding to the segmentation clock (Figure 2, S1A), global intensity analysis of timelapse flu-
960 orescence imaging was done using Fiji (70). Z-stacks were first projected based on maximum intensity [in Fiji: Image >
961 Stacks > Z Project]. Then, after maximum projection, the timeseries was obtained by plotting the z-axis profile [in
962 Fiji: Image > Stacks > Plot Z-axis Profile]. Timeseries of replicate samples were compiled in a .txt file for
963 subsequent analyses.
964

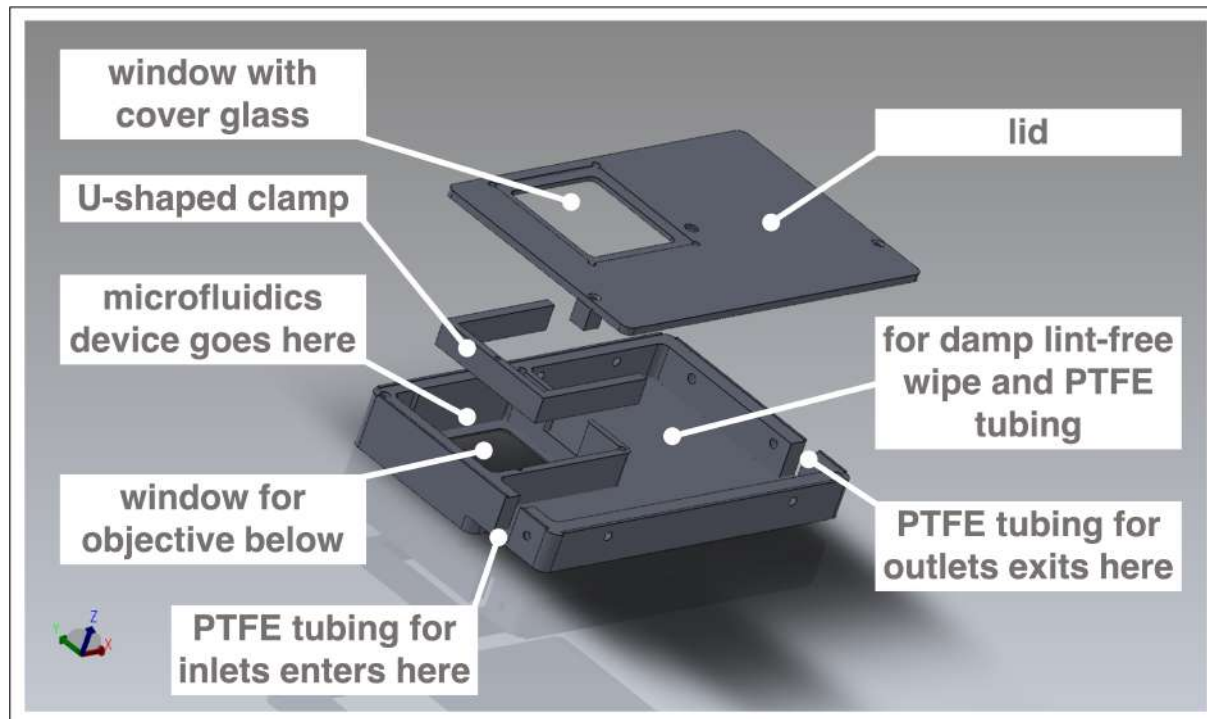


Fig. S9. Customized box to mount microfluidics device on microscope for simultaneous culture, entrainment, and live imaging. Computer-aided design (CAD) of metal box customized to hold a microfluidics device bonded to a 70 mm x 70 mm cover glass. The box fits the stage of an LSM 780 laser-scanning microscope (Carl Zeiss Microscopy). Design by Katharina Sonnen, the EMBL Mechanical Design Office, and the EMBL Mechanical Workshop.

Table S5. Pumping program of medium for entrainment to 170-min periodic pulses of drug.

Phase	Function	Rate	Volume	Remark
PH:01	LP:ST			
PH:02	RATE	60 uL/hr	140 uL	perfuse medium for 140 mins
PH:03	LP:ST			
PH:04	PS:60			pause for 60 secs
PH:05	LP:30			loop PH:04 30 times (pause for 30 mins = 60 secs × 30)
PH:06	LP:30			loop PH:02 to PH:05 30 times (total: 30 periodic pulses)
PH:07	STOP			

Table S6. Pumping program of drug/control for entrainment to 170-min periodic pulses of drug.

Phase	Function	Rate	Volume	Remark
PH:01	LP:ST			
PH:02	LP:ST			
PH:03	LP:ST			
PH:04	PS:60			pause for 60 secs
PH:05	LP:70			loop PH:04 70 times (pause for 70 mins = 60 secs × 70)
PH:06	LP:02			loop PH:04 to PH:05 2x (pause 140 mins = 70 mins × 2)
PH:07	RATE	60 uL/hr	30 uL	perfuse drug/control for 30 mins
PH:08	LP:30			loop PH:02 to PH:07 30 times (total: 30 periodic pulses)
PH:09	STOP			

Monitoring period-locking and phase-locking

Entrainment was evaluated based on period-locking and phase-locking of the signaling oscillations to the periodic drug pulses. Oscillatory components were extracted from timeseries using a wavelet analysis workflow that was developed by Gregor Mönke, which was recently implemented as a Python-based standalone software (71) available at <https://github.com/tensionhead/pyBOAT>. In this workflow, timeseries was first detrended using a sinc filter and then subjected to continuous wavelet transform. Time-resolved frequency analysis was done by cross-correlating the signal to wavelet functions of known frequencies, generating a power spectrum. A high power score was assigned to wavelets that correlated well with the signal relative to white noise. Instantaneous period and phase were extracted upon evaluation of the power spectrum along a ridge tracing wavelet with maximum power for every timepoint.

Phase dynamics of signaling oscillations, upon subjecting them to periodic perturbation, were analyzed using stroboscopic maps (38, 39, 50). Briefly, the phase difference ($\Delta\phi$) was defined as:

$$\Delta\phi = \phi(t + T_{zeit}) - \phi(t)$$

where t is the time of perturbation and T_{zeit} is the *zeitgeber* period (i.e. one cycle after time = t). $\phi(t)$ and $\phi(t + T_{zeit})$ denote the `old_phases` and their corresponding `new_phases`, respectively. The stroboscopic maps were then plotted as `new_phases` versus `old_phases` (for scheme, please refer to Figure 6A). The centroid, marking the entrainment phase (ϕ_{ent}), was determined considering only phase-locked samples (where the difference between a sample's phase at the time of the final drug pulse and its phase one drug pulse before is less than $\pi/8$). This was quantified from the average phases of the final (`old_phase`, `new_phase`) pairs considered, and the circular standard deviation (`circSD`) was calculated using the formula:

$$circSD = \sqrt{-2\ln R}$$

965 where R is the first Kuramoto order parameter. As wavelets only partially overlap the signal at the edges of the timeseries,
966 resulting in deviations from true phase values (71), the first and last pulse pairs were not considered in the generation of
967 stroboscopic maps. Polar plots were also generated summarizing the instantaneous phase of replicate samples and their first
968 Kuramoto order parameter as shown in Figure 4D, Figure 5C, and Figure S4B. The Python code is available as a Jupyter
969 notebook (.ipynb) at [https://github.com/PGLSanchez/EMBL_OscillationsAnalysis/tree/master/](https://github.com/PGLSanchez/EMBL_OscillationsAnalysis/tree/master/EntrainmentAnalysis)
970 [EntrainmentAnalysis](https://github.com/PGLSanchez/EMBL_OscillationsAnalysis/tree/master/EntrainmentAnalysis). This code uses Matplotlib (72), NumPy (73, 74), pandas (75), scikit-image (76), SciPy (77), and
971 seaborn (78).

972 Detrended timeseries of replicate samples were in some part of the study represented as a heatmap using PlotTwist
973 (47), as shown in Figure 4A. Average periods (from 650 mins to 850 mins after start of experiment) were mean-
974 while plotted using PlotsOfData (79), as shown in Figures 3C-D and Figure S2. These apps are available at [https://](https://huygens.science.uva.nl/PlotTwist/)
975 huygens.science.uva.nl/PlotTwist/ and at [https://](https://huygens.science.uva.nl/PlotsOfData/)
976 huygens.science.uva.nl/PlotsOfData/,
977 respectively.

978 Generating wavelet movies

979 Period and phase wavelet movies were generated using the Wavelet Processing and Export workflow developed by Gregor
980 Mönke, which runs on the EMBL cluster and is implemented in Galaxy with technical assistance from Jelle Scholtalbers (EMBL
981 Genome Biology Computational Support). This workflow extracts timeseries of every pixel in a timelapse movie and subjects
982 them to sinc filter-based detrending and subsequent continuous wavelet transform (71). This results in extraction of instanta-
983 neous period and phase of each pixel, recovering period and phase wavelet movies corresponding to the input timelapse movie
984 (for scheme, please refer to Figure S8A). The workflow is available at <https://github.com/tensionhead/SpyBOAT>
985 and can be used via a public Galaxy server at https://usegalaxy.eu/root?tool_id=spyboat. Settings used to
986 generate wavelet movies in this study were: sigma of 8.0, sample interval of 10 mins, period range from 100 to 250 mins, and
987 number of periods analyzed of 151.

988 Examining period gradient in 2D-assays

989 Re-oriented 2D-assays (dorsal side up) and their corresponding period and phase wavelet movies were used for the analyses.
990 Temporal evolution of the period gradient during the course of entrainment experiments was evaluated from the period
991 wavelet movies of the 2D-assays. As the period wavelet movies also contained wavelet transformations for pixels in the
992 background, a binary mask was first created to differentiate pixels corresponding to signal. To create the mask, re-oriented (and
993 registered, if necessary) timelapse movies of 2D-assays were blurred using a Gaussian blur [in Fiji: `Process > Filters`
994 `> Gaussian Blur` (sigma radius: 8, scaled units in microns)]. Then, signal was specified by thresholding [in Fiji: `Image`
995 `> Adjust > Threshold` (Default method, dark background)]. After thresholding, pixels corresponding to the signal were
996 assigned a value of 255, while those corresponding to the background were assigned a value of 0. If opposite, the values were
997 inverted [in Fiji: `Edit > Invert`]. Then, the binary mask (signal = 1 and background = 0) was created by dividing all
998 values by 255 [in Fiji: `Process > Math > Divide` (value: 255)], and was used to mask the period wavelet movie.
999

Supplementary Note 2: Theoretical methods

A. PRC correction and computation. PRCs at different entrainment periods appear shifted with respect to one another. To correct for this, we fitted the PRCs at entrainment periods $T_{zeit} = (120, 130, 140, 170)$ mins (those for which we have enough experimental data points to build a continuous curve) using 3 Fourier modes (Figure 8A1) and manually chose the phase shift optimizing their overlap for Figure 8A2. The shift values used were $(-0.45, -0.25, 0, 0.45)$ for $T_{zeit} = (120, 130, 140, 170)$ mins respectively. The data points shown in Figure 8B are used for Monte Carlo optimization (see next section). Our choice was later validated by recomputation of PRCs and comparison with data in Figure 8G. We also show corresponding PRCs in Figure S12.

B. Model. Our model (Figure S10A) is based on simple modifications of the classical Poincaré oscillator, otherwise called Radial Isochron Cycle model (RIC). The main motivation is to find the simplest possible model able to reproduce the general shape of the experimental PRC, with both a flat and a negative region, while being analytical with simple isochrons. The full description and analytical calculations for this model will be described elsewhere, here we outline the basic equations and some general properties of the model. For PRC computations, we will assume that a perturbation is a horizontal shift of magnitude A (Figure S10B).

To flatten the PRC for half the cycle, we first modify the limit cycle of the standard RIC model into an ellipse, keeping the origin as one of the foci. This is done through the introduction of a parameter λ , so that the corresponding equation of the ellipse is

$$r_{cycle} = \frac{1}{1 + \lambda \sin \theta} \quad (4)$$

combined with radial equidistant isochrons, $\dot{\theta} = 1$, where θ is the polar angle. This is however not enough to define the entire flow in the plane since one needs to specify how r converges on this cycle. We thus impose a radially uniform convergence rate equal to 1 for the radius, which leads to the following differential equation in polar coordinates:

$$\dot{r} = \dot{r}_{cycle} + r(r_{cycle} - r) \quad (5)$$

where $\dot{r}_{cycle} = -\lambda \frac{rx}{(r+\lambda y)^2}$ (again assuming $\dot{\theta} = 1$). This leads to the following equations in cartesian coordinates:

$$\dot{x} = \left(\frac{r}{r+\lambda y} - r - \frac{\lambda x}{(r+\lambda y)^2} \right) \cdot x - y = dx_{\lambda}(x, y) \quad (6)$$

$$\dot{y} = x + \left(\frac{r}{r+\lambda y} - r - \frac{\lambda x}{(r+\lambda y)^2} \right) \cdot y = dy_{\lambda}(x, y) \quad (7)$$

We name this model Elliptic Radial Isochron Cycle, or ERIC. An important feature of ERIC is that the angle in the plane is the phase of the oscillator, in particular since the phase is defined by the planar angle, the PRC following a horizontal perturbation of size A towards the right can be computed in a straightforward way and is :

$$PRC_{A,\lambda}(\theta) = \cot^{-1}(A(\csc(\theta) + \lambda) + \cot(\theta)) - \theta \quad (8)$$

As said above, the effect of introducing λ is to smoothly flatten the PRC over half of the cycle, as illustrated in Figure S11A.

We then introduce a second modification, allowing us to rescale the portion of the cycle where the PRC is flattened. We modify the equations by introducing a “speeding factor” s so that

$$\dot{\theta} = s(\theta) \quad (9)$$

This will keep isochrons radial but will change their spacing. With the elliptic limit cycle, this leads to the differential equation in cartesian coordinates

$$\dot{x} = s(\theta) dx_{\lambda}(x, y) \quad (10)$$

$$\dot{y} = s(\theta) dy_{\lambda}(x, y) \quad (11)$$

We name this class of model Elliptic Radial Isochron Cycle with Acceleration, or ERICA. For simplicity, and to keep the system analytical, we restricted ourselves first to s functions linear by piece, i.e. $s = s_* > 1$ for one sector and $s = 1$ otherwise. The sped up sector is centered at angle α and has width β , so that the modified period of the cycle is $T_{s_*} = \beta/s_* + (2\pi - \beta)$. It is also convenient to define the rescaled angular velocity $\omega_{s_*} = 2\pi/T_{s_*} = \frac{2\pi s_*}{\beta + (2\pi - \beta)s_*}$. From there, the phase of the cycle as a function of the angle θ in the plane is the simple linear transformation (defining $\theta_0 = \alpha - \beta/2$) :

$$\phi_s(\theta) = \omega_{s_*} \theta = \theta \frac{2\pi s_*}{\beta + (2\pi - \beta)s_*} \quad (12)$$

1034 for $0 < \theta < \theta_0$,

$$\phi_s(\theta) = \omega_{s_*} \left(\theta_0 + \frac{\theta - \theta_0}{s_*} \right) = \left(\theta_0 + \frac{\theta - \theta_0}{s_*} \right) \frac{2\pi s_*}{\beta + (2\pi - \beta)s_*} \quad (13)$$

1035 for $\theta_0 < \theta < \theta_0 + \beta$

1036 and

$$\phi_s(\theta) = \omega_{s_*} \left(\theta_0 + \frac{\beta}{s_*} + \theta - (\theta_0 + \beta) \right) = \left(\theta_0 + \frac{\beta}{s_*} + \theta - (\theta_0 + \beta) \right) \frac{2\pi s_*}{\beta + (2\pi - \beta)s_*} \quad (14)$$

1037 for $\theta_0 + \beta < \theta < 2\pi$. Those functions ensure that the rate of phase evolution in sector $\theta_0 < \theta < \theta_0 + \beta$ is $1/s_*$ times
 1038 the rate in the other sectors (compare θ coefficients in Eq. 12-14), that angle 0 in θ is phase $\phi_s = 0$, and that phase is
 1039 continuous so that $\phi_s(\theta_0) = \omega_{s_*}\theta_0$ and $\phi_s(\theta_0 + \beta) = (\theta_0 + \beta/s_*)\omega_{s_*}$. Notice also that for $\theta = 2\pi$ we get from Eq.14
 1040 $\phi_s(2\pi) = \left(\frac{\beta}{s_*} + 2\pi - \beta \right) \frac{2\pi s_*}{\beta + (2\pi - \beta)s_*} = 2\pi$ as expected after one full cycle.

1041 A full study of the possible behaviours of the ERICA model will be published elsewhere. Figure S11 illustrates different shapes
 1042 of PRC obtained by varying λ, s_*, α , and β independently, for various choices of sped up sectors.

1043 For optimization purpose, it is easier to numerically compute the PRC in the following way. We consider an ensemble of angles
 1044 θ_i linearly spaced on the interval $[0, 2\pi]$. We then compute the corresponding position on the ERIC limit cycle, and compute
 1045 numerically the angle $\theta_i \rightarrow A$ of the point at distance A on the right. By definition of ERICA, the PRC for each index i then is

$$PRC^{model}(\phi_s(\theta_i)) = \phi_s(\theta_i \rightarrow A) - \phi_s(\theta_i) \quad (15)$$

1046 We checked that this PRC coincides both with the one computed from the integration of the ODEs (simulating the full stro-
 1047 boscopic map procedure) and with the analytical expression. To fit the experimental PRC, we run Monte Carlo simulations to
 1048 optimize parameters A, λ, s_* , sped up sector location α and width β , and the location of the zero-phase reference point on the
 1049 cycle ϕ_0 . We minimize χ^2 :

$$\chi^2 = \sum_i \frac{(PRC_i^{corr} - PRC_i^{model})^2}{\sigma^2}, \quad (16)$$

1050 where PRC_i^{corr} are data points of the corrected experimental PRC and σ is the noise, estimated as the root mean square error
 1051 of a Fourier fit to data (see Figure 8A). We use Markov chains to generate distributions of parameters and take the average
 1052 values to plot the model limit cycle and PRC. The optimized parameter values are: $A = 0.43, \lambda = 0.53, s_* = 5.64, \alpha = 1.51\pi,$
 1053 $\beta = 1.15\pi, \phi_0 = 1.17\pi$.

1054 **C. Evidence for intrinsic period changes.** The PRC shifts are interpreted as change of period of the intrinsic oscillator
 1055 because of entrainment.

1056 We first checked that such PRC shifts are really needed to explain data. To do this, we computed an average PRC by only
 1057 taking into account entrainment periods between 130 and 150 mins. If we assume there is no period change, we can compute
 1058 the maximum entrainment period compatible with such PRC, and found it is equal to 170 mins. However it is clear from our
 1059 data that we can go beyond this entrainment period, confirming the shift of PRC, in agreement with a change of intrinsic period.
 1060 We further have two evidences for such changes from release experiments. In those experiments, we entrain the oscillators for 2
 1061 cycles at 170 mins, then let it go, and measure both the phase and instantaneous periods of the oscillator (Figure S5). When we
 1062 measure the period, we first find it takes several cycles to come back to the intrinsic period, showing a long lived effect, unlikely
 1063 coming from some artefact of period computation (Figure S5). A more direct way to estimate period change is to compute the
 1064 return maps after the last pulse of DAPT. In Figure S12A we consider all release experiments, which were done with *zeitgeber*
 1065 period of 170 mins. We take the phase one full cycle after the last pulse, and compute the return map from this phase (so for
 1066 the first full cycle with no pulses). From this, we can compute the length of the cycle to have an average phase difference of 0
 1067 (corresponding to the period two full cycles after the last pulse). We found a cycle length of 150 minutes, compatible with the
 1068 instantaneous period measurement and incompatible with a fast return to a 140 minutes intrinsic period.

1069 We further show the Arnold tongue computed numerically with a similar PRC (1 : 1 entrainment region) and corresponding
 1070 isophases assuming a fixed intrinsic period of 140 minutes in Figure S12B. We see much narrower width clearly incompatible
 1071 with the data, again confirming the need for an intrinsic period change.

1072 The last evidence is both more indirect but more mathematically grounded. It comes from the sigmoidal shape of the experi-
 1073 mental entrainment phase as a function of *zeitgeber* period (Figure 7B, 8E). In a nutshell, flatness of this curve is incompatible
 1074 with the classical PRC theory, but can be easily explained if the internal period T_{osc} changes linearly with T_{zeit} .

1075 To see this, we start with the classical condition for stability of the entrainment phase (see e.g. (49))

$$-1 < \left. \frac{dPTC}{d\phi} \right|_{\phi=\phi_{ent}} < 1 \quad (17)$$

1076 or equivalently :

$$-2 < \left. \frac{dPRC}{d\phi} \right|_{\phi=\phi_{ent}} < 0 \quad (18)$$

1077 Now we also have by definition of the entrainment phase ϕ_{ent} :

$$PRC(\phi_{ent}) = T_{osc} - T_{zeit} \quad (19)$$

1078 This equation defines in an implicit way a function $\phi_{ent}(T_{zeit})$, and the corresponding experimental curve is plotted in Figure
1079 8E for our data. Taking the derivative on both sides with respect to the *zeitgeber* period, we get (first assuming a constant
1080 intrinsic period):

$$\left. \frac{dPRC}{d\phi} \right|_{\phi=\phi_{ent}} \frac{d\phi_{ent}}{dT_{zeit}} = -1 \quad (20)$$

1081 This allows to implicitly define the curve $\phi_{ent}(T_{zeit})$ with the help of the *PRC*:

$$\frac{d\phi_{ent}}{dT_{zeit}} = - \left(\left. \frac{dPRC}{d\phi} \right|_{\phi=\phi_{ent}} \right)^{-1} \quad (21)$$

1082 There is a geometric interpretation here : the curve $\phi_{ent}(T_{zeit})$ is in fact a $+\pi/2$ rotation of the *PRC*! This can be seen here
1083 because Eq. 21 combines a the mirror image of the *PRC* along the *y* axis (minus sign) with a mirror image along the first
1084 diagonal (power -1 which corresponds to the inversion function exchanging ϕ and *PRC* ($\phi, PRC(\phi) \rightarrow (PRC(\phi), \phi)$). We
1085 know from classical group theory that two mirror images give one rotation with an angle equal to twice the angle between the
1086 axis (so here $2\pi/4 = \pi/2$). For instance, if the *PRC* is sinusoidal, $\phi_{ent}(T_{zeit})$ looks itself like (half a period) of a vertical
1087 sinusoidal, as can be clearly seen e.g. in (51). In Figure 8C, we further illustrate this rotation using the *PRC* computed from
1088 the data: the *PRC* rotated by $\pi/2$ is compared with the curve $\phi_{ent}(T_{zeit})$ computed numerically from it, showing perfect
1089 agreement.

1090 Now, since the geometry of the *PRC* is constrained by Eq. 18, this in turn imposes geometric constraints on $\phi_{ent}(T_{zeit})$, e.g.
1091 combining Eqs. 18-21, we get

$$\frac{d\phi_{ent}}{dT_{zeit}} > \frac{1}{2} \quad (22)$$

1092 This defines an absolute, *minimum* slope of the curve $\phi_{ent}(T_{zeit})$ (counting here time in units of intrinsic period T_{osc}). How-
1093 ever, we see experimentally in Figure 8E that the entrainment phase is becoming almost constant for low and high values of the
1094 entrainment period, indicating a zero slope, which thus is theoretically impossible from Eq. 22.

1095 Now the simplest way to reconcile this observation with this calculation is to assume that the intrinsic period T_{osc} in fact
1096 depends on the *zeitgeber*. We then get a generalized version of Eq. 20 with changing intrinsic period

$$\left. \frac{dPRC}{d\phi} \right|_{\phi=\phi_{ent}} \frac{d\phi_{ent}}{dT_{zeit}} = \frac{dT_{osc}}{dT_{zeit}} - 1 \quad (23)$$

1097 giving the new implicit definition

$$\frac{d\phi_{ent}}{dT_{zeit}} = \left(\frac{dT_{osc}}{dT_{zeit}} - 1 \right) \left(\left. \frac{dPRC}{d\phi} \right|_{\phi=\phi_{ent}} \right)^{-1} \quad (24)$$

1098 and the new constraint (assuming $\frac{dT_{osc}}{dT_{zeit}} < 1$, which is expected if the intrinsic period dependency with respect to the *zeitgeber*
1099 is relatively small)

$$\frac{d\phi_{ent}}{dT_{zeit}} > \frac{(1 - \frac{dT_{osc}}{dT_{zeit}})}{2} \quad (25)$$

1100 In this situation, we see that when $\frac{dT_{osc}}{dT_{zeit}} \sim 1$, the right hand side of both Eqs. 24-25 can become arbitrarily small, so that one
1101 can get $\frac{d\phi_{ent}}{dT_{zeit}} \sim 0$ as observed experimentally in Figure 8E. This effect will also come with a considerable enlargement of the
1102 Arnold tongue as discussed below. Also we notice that $\frac{dT_{osc}}{dT_{zeit}} \sim 1$ could be indicative of a mechanism where the oscillator
1103 adapts its intrinsic period (here to the *zeitgeber* period).

1104 Practically, we obtain the $T_{osc}(T_{zeit})$ dependency by fitting the stroboscopic maps and entrainment phase from all experiments
1105 with 2.0 uM DAPT, using the PTC of our optimized model (Figure S12D-E). The values of T_{osc} are shown as data points in
1106 Figures 8D and S12F.

1107 **D. Arnold tongue computations.** To build the Arnold tongues, we first need to interpolate the period changes for period
1108 values not used in entrainment experiments. We used cubic spline interpolation to draw Figure 8D. For periods outside of the
1109 range of entrainment, in the absence of data some arbitrary choices have to be made. We know experimentally that entrainment
1110 does not occur below ~ 120 mins and above ~ 200 mins which indicates that $\frac{dT_{osc}}{dT_{zeit}}$ is becoming smaller around those *zeitgeber*
1111 periods. More biologically, this indicates that the system does not adjust to any entrainment period. Again some arbitrary
1112 choices have to be made, but based on those constraints and our own interpolation, a cut-off for T_{osc} of $\pm 20\%$ of the natural
1113 period of 140 mins was assumed, and is further consistent with the relative period changes observed experimentally in zebrafish
1114 segmentation clock mutants (20) and theoretically derived from delayed coupled models (80). With such cut-off, the obtained
1115 entrainment range of *zeitgeber* periods is from 118 to 200 mins.
1116 Computation of Arnold tongue and isophases in Figure 8F was done by iterations of the return map Eq. 2 and detection of fixed
1117 points, using as the intrinsic period the interpolation and extrapolation showed in Figure S12F.
1118 Lastly, we can use this model to compute entrainment phase for different DAPT concentrations. For the main concentration of
1119 2.0 uM DAPT, we have the optimized amplitude of perturbation $A = 0.43$. Assuming that the DAPT concentration is reflected
1120 in the strength of perturbation, we can find cross-sections of the isophases at different values of A to have excellent agreement
1121 with experiments, as illustrated in Figure S12G. We take $A = 0.55$ for 3.0 uM, $A = 0.31$ for 1.0 uM, and $A = 0.13$ for 0.5 uM
1122 DAPT, as shown on the Arnold tongue in Figure 8F. We capture both the presence/absence of entrainment and the $\phi_{ent}(T_{zeit})$
1123 relation. In particular, we see that for lower DAPT concentrations, the range of entrainment is smaller but we still get plateaus
1124 in entrainment phase consistent with the change of period we computed.

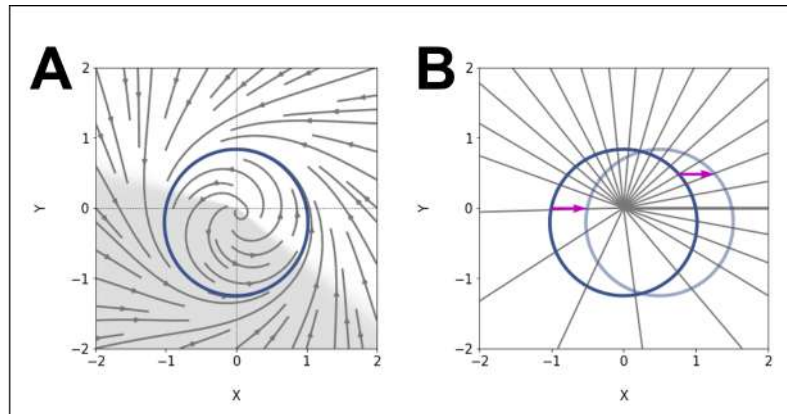


Fig. S10. ERICA model. (A) Our model consists of an elliptic limit cycle (blue) with increased angular velocity in one sector (shaded region). (B) The effect of such acceleration is to change the spacing of isochrons (radial lines). We compute the PRC of the model by introducing a perturbation (arrow) at points on the limit cycle and looking at the starting and ending isochrons.

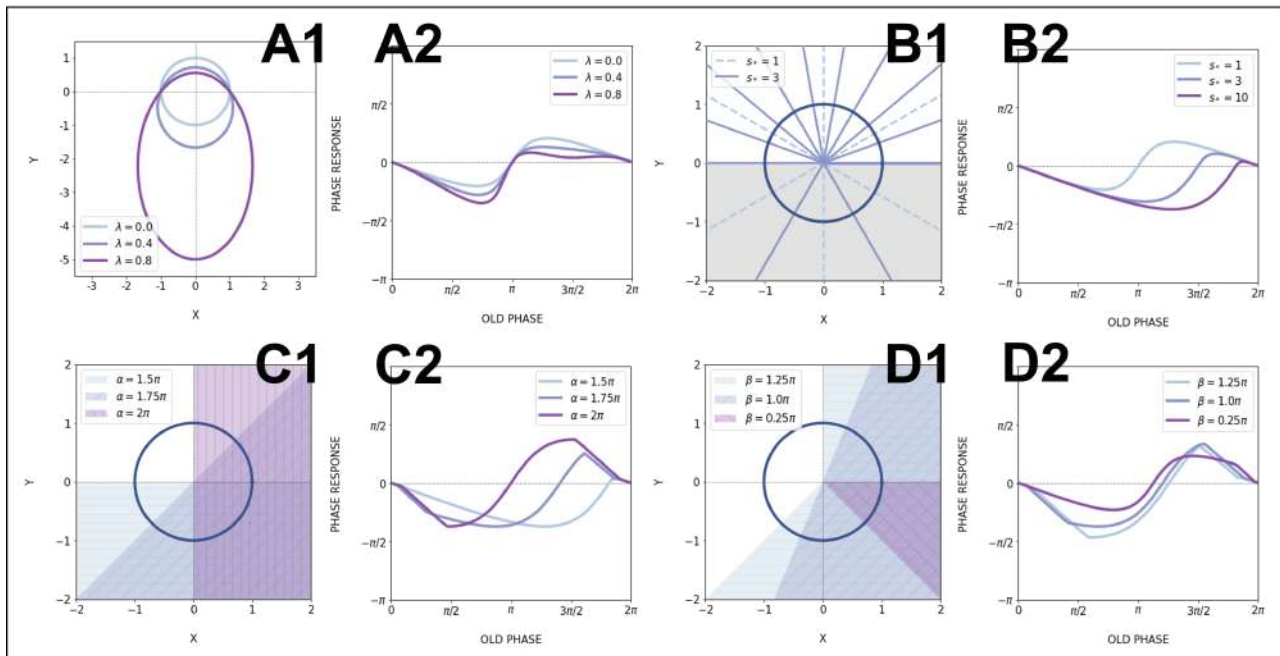


Fig. S11. Effects of model parameters on the PRC. (A) Effect of eccentricity λ : (A1) Increasing λ makes the limit cycle more elongated, while keeping the upper focus at the origin. (A2) The positive part of the PRC is then flattened; for all PRCs here $s_* = 1$ (no acceleration). (B) Effect of speeding up s_* : (B1) When s_* is increased, the spacing between isochrons in the sped up region increases, so this region contains less and less isochrons. Shown here is the case when the acceleration happens in the lower half-plane ($\alpha = 1.5\pi$, $\beta = \pi$), which is shaded in grey. (B2) The effect on the PRC is to shrink the portion where the oscillator is sped up, thus emphasizing the other part of the curve. Here $\lambda = 0$. (C, D) Effects of the sped up sector parameters α, β : the location and width of the sector determine which parts of the PRC get rescaled. (C1) The shaded regions are sectors with different values of α , and $\beta = \pi$. (C2) The corresponding PRCs with $\lambda = 0$, $s_* = 10$. (D1) Sped up sectors located at $\alpha = 15/8\pi$ with different widths β . (D2) The corresponding PRCs for the case $\lambda = 0$, $s_* = 10$. All PRCs in this figure were computed with perturbation amplitude $A = 0.6$.

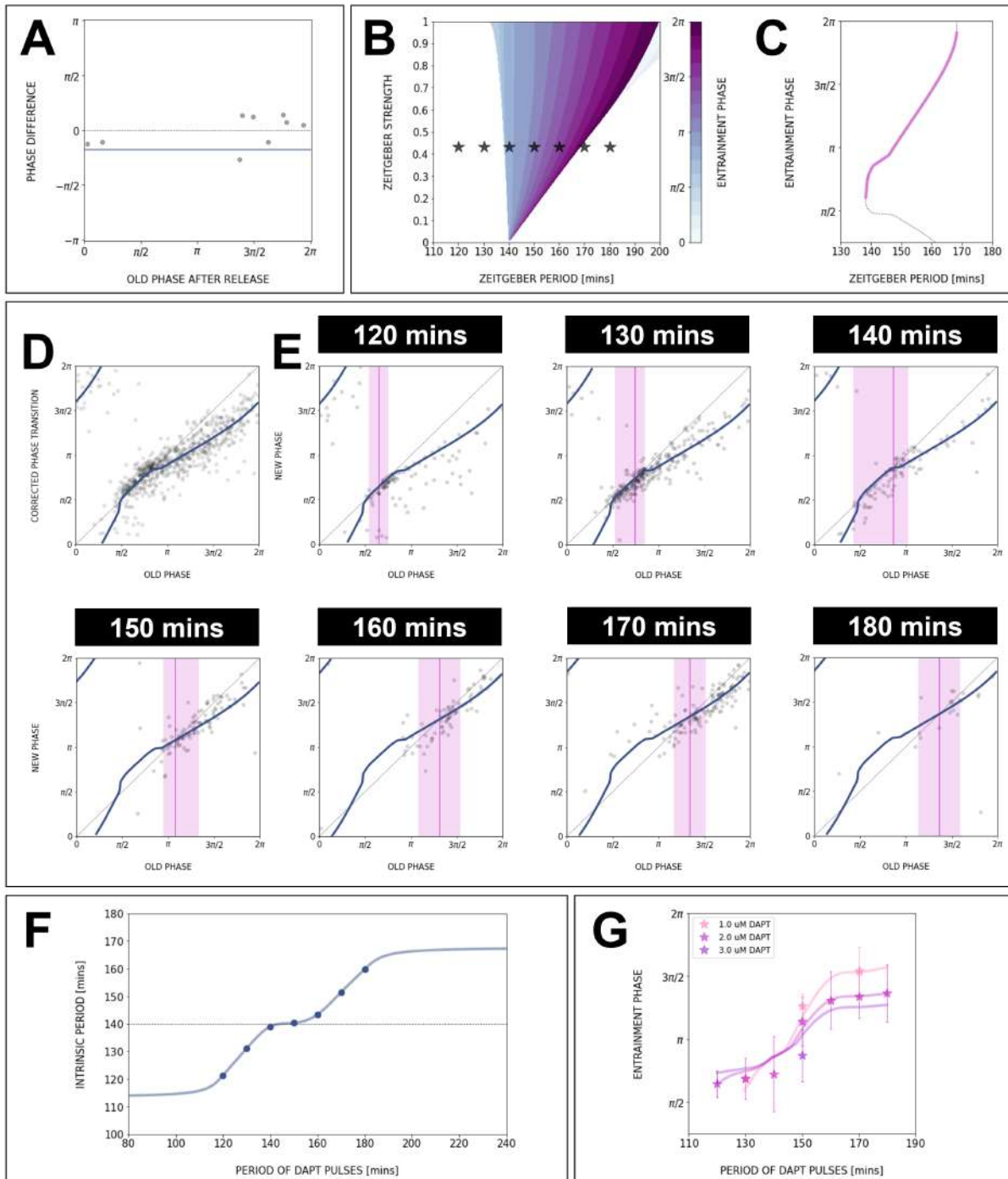


Fig. S12. Data for the PRC/PTC, stroboscopic maps and entrainment phase can be fully captured with our model and changing intrinsic period. (A) Stroboscopic map data from release experiments allows to estimate the intrinsic oscillation period during entrainment. With $T_{osc} = 150$ mins, the phase difference between the end and the beginning of the first full cycle with no perturbations is on average 0 (2π). The data points are from different release experiments with $T_{zeit} = 170$ mins. If the natural period of 140 mins is used, the average phase difference is -0.17π (solid line). (B, C) Constant intrinsic period T_{osc} is not consistent with experimental data: (B) The 1 : 1 Arnold tongue, computed using our model and $T_{osc} = 140$ mins, is much narrower than the experimental entrainment range. Stars correspond to experimental conditions (T_{osc} , A) where entrainment was observed. (C) Entrainment phase $\phi_{ent}(T_{zeit})$ numerically computed with the optimized PRC from Figure 8C, assuming constant $T_{osc} = 140$ min (which also corresponds to a cross-section of the isophases in B). Clearly, the slope of the curve is much higher than in the data. For comparison, we also plot the Figure 8C PRC rotated by $\pi/2$, showing perfect overlap. (D) PTC of the optimized model (equivalent to the PRC shown in Figure 8C). (E) Using the PTC from D, we fit the stroboscopic maps data for all periods T_{zeit} by choosing the $T_{osc}(T_{zeit})$ that gives the right detuning. The narrow magenta lines indicate the entrainment phase, the fixed point of each fitted stroboscopic map. The shaded magenta regions show the experimental range for entrainment phase. (F) Extrapolation of the intrinsic oscillator period T_{osc} as a function of zeitgeber period T_{zeit} . (G) Cross-sections of the isophases in Figure 8F, calculated with the model and the extrapolated curve for $T_{osc}(T_{zeit})$, give excellent agreement with the entrainment phase data for different concentrations of DAPT.

1125 **Supplementary Note 3: Movies**

- 1126 • E10.5 2D-assay, expressing LuVeLu, subjected to 130-min periodic pulses of DMSO control, with corresponding period
1127 and phase wavelet movies, available at [https://github.com/PGLSanchez/EMBL-files/blob/master/
1128 MOVIES/SO_2.0D_130mins_CTRL.avi](https://github.com/PGLSanchez/EMBL-files/blob/master/MOVIES/SO_2.0D_130mins_CTRL.avi)
- 1129 • E10.5 2D-assay, expressing LuVeLu, subjected to 130-min periodic pulses of 2 uM DAPT, with corresponding period
1130 and phase wavelet movies, available at [https://github.com/PGLSanchez/EMBL-files/blob/master/
1131 MOVIES/SO_2.0D_130mins_DAPT.avi](https://github.com/PGLSanchez/EMBL-files/blob/master/MOVIES/SO_2.0D_130mins_DAPT.avi)
- 1132 • E10.5 2D-assay, expressing LuVeLu, subjected to 170-min periodic pulses of DMSO control, with corresponding period
1133 and phase wavelet movies, available at [https://github.com/PGLSanchez/EMBL-files/blob/master/
1134 MOVIES/SO_2.0D_170mins_CTRL.avi](https://github.com/PGLSanchez/EMBL-files/blob/master/MOVIES/SO_2.0D_170mins_CTRL.avi)
- 1135 • E10.5 2D-assay, expressing LuVeLu, subjected to 170-min periodic pulses of 2 uM DAPT, with corresponding period
1136 and phase wavelet movies, available at [https://github.com/PGLSanchez/EMBL-files/blob/master/
1137 MOVIES/SO_2.0D_170mins_DAPT.avi](https://github.com/PGLSanchez/EMBL-files/blob/master/MOVIES/SO_2.0D_170mins_DAPT.avi)

1138 **Supplementary Note 4: Text files**

- 1139 • Text (.txt) files containing timeseries from microfluidics-based entrainment experiments, available at [https://
1140 github.com/PGLSanchez/EMBL-files/tree/master/ENTRAINMENT-timeseries](https://github.com/PGLSanchez/EMBL-files/tree/master/ENTRAINMENT-timeseries)